AERODYNAMIC OPTIMIZATION OF INLET DESIGN FOR HIGH BYPASS RATIO TURBOFAN

A THESIS SUBMITTED TO
THE GRADUATE SCHOOL OF NATURAL AND APPLIED SCIENCES
OF
MIDDLE EAST TECHNICAL UNIVERSITY

BY

YAĞIZ KAPLAN

IN PARTIAL FULFILLMENT OF THE REQUIREMENTS
FOR
THE DEGREE OF MASTER OF SCIENCE
IN
AEROSPACE ENGINEERING

JANUARY 2024

Approval of the thesis:

AERODYNAMIC OPTIMIZATION OF INLET DESIGN FOR HIGH BYPASS RATIO TURBOFAN

submitted by **YAĞIZ KAPLAN** in partial fulfillment of the requirements for the degree of **Master of Science** i**n Aerospace Engineering, Middle East Technical University** by,

Prof. Dr. Halil Kalıpçılar
Dean, **Graduate School of Natural and Applied Sciences** _____

Prof. Dr. Serkan Özgen
Head of the Department, **Aerospace Engineering** _____

Prof. Dr. Yusuf Özyörük
Supervisor, **Aerospace Engineering, METU** _____

Examining Committee Members:

Prof. Dr. Sinan Eyi
Aerospace Engineering, METU _____

Prof. Dr. Yusuf Özyörük
Aerospace Engineering, METU _____

Assoc. Prof. Dr. Nilay Sezer Uzol
Aerospace Engineering, METU _____

Assoc. Prof. Dr. Mustafa Kaya
Aerospace Engineering, Ankara Yıldırım Beyazıt Uni. _____

Assist. Prof. Dr. Onur Baş
Mechanical Engineering, TED Uni _____

Date: 22.01.2024

I hereby declare that all information in this document has been obtained and presented in accordance with academic rules and ethical conduct. I also declare that, as required by these rules and conduct, I have fully cited and referenced all material and results that are not original to this work.

Name Last name : Yağız Kaplan

Signature :

ABSTRACT

AERODYNAMIC OPTIMIZATION OF INLET DESIGN FOR HIGH BYPASS RATIO TURBOFAN

Kaplan, Yağız
Master of Science, Aerospace Engineering
Supervisor : Prof. Dr. Yusuf Özyörük

January 2024, 95 pages

The inlet of the engine of an aircraft must allow the required amount of air pass into the engine with the minimum possible pressure losses and highest possible smoothness at a wide range of flight conditions such as climb and cruise situations. Moreover, the presence of the engine nacelle has an impact on the pressure distribution over the installation area on the aircraft. Therefore, the nacelle housing the engine core should be designed in the most optimum way against the adverse conditions that may occur. In this thesis, the inlet of a turbofan engine nacelle from literature, called the baseline geometry, is studied for optimal shape based on the pressure recovery ratio and drag coefficient values. The commercial computational fluid dynamics solver Fluent is used for flow solutions, and a Multi-Objective Genetic Algorithm (MOGA) is used for optimization. The optimization results indicate that compared to those of the baseline geometry, the pressure recovery ratio by the fan is increased by 3.97% and 3.02% at the climb and cruise conditions, respectively. Also, the drag coefficients are reduced by 11.43% and 17.32% at these conditions, respectively. The study has shown that the employed

optimization approach utilizing the MOGA optimization fed by CFD solutions has proven a useful one for turbofan inlet shape design.

Keywords: Nacelle Optimization, Aerodynamics, Multi-Objective Genetic Algorithm, Pressure Recovery

ÖZ

YÜKSEK BYPASS ORANLI TURBOFAN İÇİN GİRİŞ TASARIMININ AERODİNAMİK OPTİMİZASYONU

Kaplan, Yağız
Yüksek Lisans, Havacılık ve Uzay Mühendisliği
Tez Yöneticisi: Prof. Dr. Yusuf Özyörük

Ocak 2024, 95 sayfa

Bir uçağın motor girişi, tırmanma ve seyir durumları gibi çok çeşitli uçuş koşullarında, mümkün olan en az basınç kaybı ve mümkün olan en yüksek pürüzsüzlük ile gerekli miktarda havanın motora geçmesine izin vermelidir. Ayrıca motoru koruyan bölgenin varlığının, uçak gövdesi üzerinde bulunan kısımdaki basınç dağılımına büyük etkisi vardır. Bu nedenle motor çekirdeğini barındıran motor kaportasının, oluşabilecek olumsuz koşullara karşı en optimum şekilde tasarlanması gerekmektedir. Bu tezde, literatürde yer alan ve temel geometri olarak adlandırılan bir turbofan motor kaportasının girişinin, basınç geri kazanım oranı ve sürüklenme katsayısı değerlerine dayalı olarak en uygun şekle getirilmesi incelenmiştir. Akış çözümleri için ticari hesaplamalı akışkanlar dinamiği çözücüsü Fluent kullanılır ve optimizasyon için Çok Amaçlı Genetik Algoritma (MOGA) kullanılır. Optimizasyon sonuçları, temel geometriyle karşılaştırıldığında fanın basınç geri kazanım oranının tırmanma ve seyir koşullarında sırasıyla %3,97 ve %3,02 arttığını göstermektedir. Ayrıca sürükleme katsayıları bu koşullarda sırasıyla %11,43 ve %17,32 oranında azaltılmıştır. Çalışma, CFD çözümleri tarafından beslenen MOGA optimizasyonunu kullanan yaklaşımın, turbofan giriş şekli tasarımı için yararlı olduğunu kanıtlamıştır.

Anahtar Kelimeler: Nacelle Optimizasyonu, Aerodinamik, Çok Amaçlı Genetik Algoritma, Basınç Geri Kazanımı

To my family

ACKNOWLEDGMENTS

I wish my deepest feelings to my thesis supervisor Prof. Dr. Yusuf Özyörük for giving me this opportunity to work with him and providing me flexibility throughout the thesis study.

I also would like to thank my colleagues and friends for their support and friendship. I have always had the support of these people in challenging myself against difficulties.

I would also like to thank all the lecturers and civil servants at work for providing me with a suitable working environment.

Finally, I would like to express my love to my family, who have always raised me well since I was born, spared nothing, and have always been by my side in facing difficulties.

TABLE OF CONTENTS

LIST OF TABLES

TABLES

LIST OF FIGURES

FIGURES

LIST OF ABBREVIATIONS

ABBREVIATIONS

CFD	Computational Fluid Dynamics
FVM	Finite Volume Method
LHS	Left Hand Side
MOGA	Multi-Objective Genetic Algorithm
ODE	Ordinary Differential Equations
PDE	Partial Differential Equations
PR	Pressure Recovery
RANS	Reynolds Averaged Navier-Stokes
RHS	Right Hands Side
RSM	Response Surface Method
TM	Turbulence Model

LIST OF SYMBOLS

SYMBOLS

α	Angle of Attack
K	Turbulent Kinetic Energy
M	Mach Number
$\dot{m}$	Mass Flow Rate
μ	Dynamic Viscosity
ν	Kinematic Viscosity
ρ	Density
P_t	Total Pressure
R	Gas Constant
S	Sutherland Temperature
T_{ref}	Reference Temperature
δ_{ij}	Reynolds-Averaged Strain Rate Tensor
V_∞	Free Stream Velocity

CHAPTER 1

INTRODUCTION

Compared to the past, airplanes are one of the most important means of transportation today, and the field of aviation is open to more innovative ideas, developments, and improvements. Aircraft might be categorized as commercial, military, training, cargo, etc. Among these range and endurance of passenger transport and cargo aircraft are usually higher than the others for reasons of economical and safe operations. Since commercial aircraft can travel thousands of kilometers, one of the most important things to consider for them is fuel consumption. Therefore, airplanes cruising usually at high subsonic speeds employ turbofan engines due to their superior propulsive. The nacelle air inlet is one of the components of a turbofan engine. This component is an important player in propulsive efficiency and fuel consumption of the engine. The inlet must let sufficient air mass flow into the engine with lowest possible losses and disturbances. Otherwise, problems such as more fuel consumption, uneven loading, vibration, and noise may result. For this reason, the nacelle air inlet design is performed by taking all these points into consideration.

1.1 Background

The nacelle inlet shape is crucial for the overall efficiency of a turbofan engine. This is because the working air mass flow gets into the engine through this component. The amount of mass flow must be sufficient. In addition, this mass flow must reach the fan of a turbofan engine as uniform as possible, both radially and circumferentially, with minimal unsteady disturbances. Moreover, the total pressure loss and thereby its adverse effect on the overall propulsive efficiency must be minimum. The nacelle shape also has an impact on the aerodynamic

characteristics of the installation area on the airplane. Increased drag due to the presence of the causes an increment in the overall drag of the aircraft, hence an increase in fuel consumption [1]. Therefore, the drag force coming over the nacelle body should also be reduced.

Determining the flow characteristics through the nacelle is a difficult and costly task in a design cycle. This is because any time a shape change or modification is carried out, a new model must be constructed and tested. Computational methods employing solutions of flow conversation equations, such as Navier-Stokes equations, on the other hand are today much less costly and routinely used in aerodynamic shape optimization.

Figure 1.1. Example of a Nacelle Body [2]

1.1.1 Intake Flow Physics

Flow passing through a turbofan nacelle (e.g. Figure 1.1) is quite complex for some reasons. When the engine is running while the aircraft is on the runway, vortices begin to form between the nacelle and the ground which is caused by the interaction of the airflow leaving the nacelle and the air striking the ground, as shown for example in Figure 1.2. This is one of the things that are not desirable

since vortices can adversely affect the engine performance as well as that of the aircraft such as reducing the lift force [3]. The curvature of the inlet wall of the nacelle affects the direction of the incoming air flow and thereby its characteristics, and therefore is considered as an important parameter. The level of total pressure decrease through the intake depends on the flow phenomena such as wall friction, flow separation, and perhaps shock waves [4]. The second crucial parameter is the nacelle drag coefficient. Just like any surface, the nacelle shape creates a drag force due to the flow passing over it. The curved nacelle shape should be designed carefully so that the flow through it occurs as smoothly as possible, without much drag force creation. Therefore, the complex curved shapes of nacelles are determined through some shape optimization procedures.

Figure 1.2. Example of Ground Vortices on Nacelle Body [5]

1.1.2 Literature Survey

As has already been expressed the nacelle, which surrounds and protects an engine, has importance in terms of its efficiency as well as the overall performance of an aircraft. Recently, the nacelle shape optimization studies appeared in literature with the aim of making the air flow draws into the engine smoother and more regular. In this section, literature work is discussed.

1.1.2.1 Shape Optimization Studies

There are many numerical studies about the researching the optimal shape for the nacelle design. In 2016, Anisimov and Savelyev [25] performed a numerical analysis on airplane propulsion system to find an optimal shape where the numerical analysis is based on Reynolds-Averaged Navier-Stokes equations. Their methodology was focused on the external aerodynamics of the power plant since the internal aerodynamics are only used to optimize the external aerodynamics of power plant and does not require other consortium participants. In their optimization process, commercial optimization program called Dakota is used with the efficient global optimization (EGO) algorithm using a surrogate model which is constructed by kriging method [25]. One of their important findings is that the drag coefficient reduction at cruise stage. After the optimization, drag coefficient is reduced 2.5% according to the baseline model. Secondly, the optimal nacelle design has a shorter length, a larger diameter and more rounded nose than the initial design. The most important outcome of their study is that the weak interference between the nozzle and inlet section in optimization. Therefore, there should be two independent parts when designing the nacelle body.

Also in 2016, Savelyev, Matyash, and Shenki [26] performed an analysis on blended wing body (BWB) aircraft to optimize the position of the nacelle and performance of the aircraft. Their numerical approach is solving the RANS to calculate the aerodynamic characteristics of the aircraft and nacelle body. Their main is goal is to lessen the thrust losses which is the difference between the thrust of the isolated engine and the thrust of the engine installed on the aircraft [26]. Turbulent flow solver and optimization algorithm are selected as Spalart-Allmaras and EGO respectively. Similarly, the found out that the optimization of inlet and nozzle section should be performed independently. Firstly, nozzle section should be designed and then the inlet section design should be generated. The important result of this study includes that the optimal position of the nacelle on BWB

aircraft reduces the thrust losses by 6.5% and 3.5% at cruise and take-off stages respectively according to the baseline model.

Moreover, in 2016, Li and Zhong [27] studied a similar subject where their objective is to increase the laminar area ratio and the maximum Mach number observed on the nacelle surface. In their solution process, compressible RANS with steady equations are selected. To improve the optimization efficiency, multi-island genetic algorithm [28] is utilized to predict transition and drag force so that the numerical simulation cost and period can be reduced significantly. They focused on 2-Dimensional optimization of the non-uniform rational splines [29] to reduce the computational costs and save time. And they found out that the optimized nacelle has 7% increased laminar area ratio and 6.5% less drag coefficient at cruise conditions. Also, the maximum Mach number observed in the nacelle surface is dropped from 1.31 to 1.09 which is a significant fall.

As stated in other studies where the optimizations of the inlet and nozzle parts are not the same, not all studies only examine the nacelle in its entirety. Some of them only examine the inlet part and focus on optimization by varying the curvature design of the inlet. Moreover, mathematical descriptions of geometries are involved in many shape optimization problems found in literature searches. Curvatures in a specific geometry can be defined by polynomials and splines. According to the Savelyev, Mikhaylov and Zlenko [30], they created the geometry of the inlet section of nacelle by using a non-uniform rational B-spline (NURBS) method, which is a type of spline function that allows for flexible and smooth interpolation of discrete points [31]. They found that the optimal inlet design depends on four main parameters which are lip thickness coefficient, curvature radius of inlet, throat diameter, and midsection diameter with its position which are also told in [26]. The second result they found that the optimal inlet shape reduces the external drag coefficient of the nacelle by about 20% and increases the effective thrust by about 4% at cruise conditions.

Although there are many studies on a similar subject, the optimization techniques and methods used in experiments differ from each other. In another work from 2010, Wang et al. [32] presented a method for optimization of the location of the nacelle and pylon on a civil transport aircraft with wing-body configuration. In their case, they wanted the minimize the drag coefficient and the interference drag. In optimization scheme, another optimization type is used which is called as advanced particle swarm optimization (PSO) to optimize the nacelle/pylon position. Advanced Particle Swarm Optimization (PSO) is a variant of particle swarm optimization that uses an improved velocity update strategy to reach the optimal point. PSO was developed in 2003 by Eberhart and Shi [33] and has been shown to be effective in a variety of optimization problems. In their results, they found that the optimal position improves the lift-to-drag ratio by 1.9% at cruise and 2.2% at take-off conditions compared to the main shape. Also, the interference drags between the nacelle and wings drop 9.3% and 10.7% at cruise and take-off regimes, respectively.

Another work from 2016 [34] states that the laminar area ratio extended to 36% and the drag coefficient reduces approximately 2.1% in the shape of transonic natural laminar flow nacelles. After the geometric parameterization of axis-symmetric nacelle, a four-equation transition model for transition prediction is used, and the differential evolution algorithm combined with the differential evolution algorithm combined with RBF surrogate model. The differential evolution algorithm is a population-based stochastic optimization method that uses mutation, crossover, and selection operators to generate new solutions [35]. The RBF surrogate model is a type of approximation model that uses radial basis functions to interpolate the objective function values at sampled points [36].

As for the studies using the MOGA algorithm embedded in Ansys, El-Sayed et al. [37] used MOGA optimization technique to optimize the aerodynamic performance of a nacelle for a civil aircraft. The objective functions were drag reduction and maximization of lift-to-drag ratio. The study found that MOGA was able to find a Pareto-optimal solution that significantly improved the aerodynamic performance

of the nacelle. The observation of reduction in drag by 15% is observed. It is also found that MOGA was able to increase the lift-to-drag ratio of the nacelle by 5%.

Another work from 2016, Kumar et al. [38] used also MOGA to optimize the nacelle-pylon configuration of a civil aircraft. The objective functions were drag reduction, lift-to-drag ratio maximization, and minimization of structural weight. The study found that MOGA was able to find a Pareto-optimal solution between these three input parameters that significantly improved the aerodynamic performance of the nacelle-pylon configuration. The MOGA optimization process achieved a remarkable 12% reduction in drag compared to the baseline design, 5% reduction in structural weight and 9% increment in lift-to-drag ratio.

Also, similar subject studied by Liu et al. in 2016 [39] aimed to increase the lift-to-drag ratio as well by reducing the drag coefficient. They used MOGA optimization algorithm as with the combination of kriging interpolation technique which is a multi-objective optimization algorithm that combines MOGA with Kriging interpolation. MOGA is a gradient-based algorithm that is well-suited for problems with smooth objective functions, while Kriging is a non-parametric interpolation method that can be used to approximate complex objective functions [40]. The combination of these two algorithms allows MOGA-Kriging to effectively solve a wide range of multi-objective optimization problems. They found out that the MOGA-kriging interpolation method was able to reduce drag by up to 10% while maintaining structural integrity. Also, the MOGA-kriging interpolation method was able improve the lift-to-drag ratio by up to 5%.

These studies show that the nacelle structure can be optimized both as a whole and by examining the inlet and nozzle parts separately. Different optimization techniques used in these studies are also explained briefly. Moreover, these studies display that MOGA which is embedded on commercial flow problem solver Ansys Fluent is a powerful tool for improving the aerodynamic performance of nacelles. MOGA can find Pareto-optimal solutions that balance multiple objective functions, making it a valuable tool for nacelle design.

1.1.2.2 Intake Flow Computations

There are many studies found in the literature that studied the flows through nacelle body numerically and experimentally. However, since it is impossible to constantly create and try a new design for aircraft nacelle design in daily life, it has been observed that shape optimization studies have been done computer based due to given reasons. Moreover, experimental analysis is more expensive than the computer-based analysis, and experimental tests required so much power for operation. Therefore, numerical applications were the priority for studies observing for optimal shape design. Navier-Stokes equations are the most known and common approach for solving the flow behavior over the nacelle surface. Even if one of most effective way to compute the turbulent flow behavior in any shape is Direct Numerical Simulation (DNS), the number of mesh that I have used in my thesis is so high. So, it is not appropriate for me to use because of computing time on each mesh.

Therefore, Reynolds Averaging method is used in CFD simulations to solve the approximate results of Navier-Stokes equations. However, averaging the Navier-Stokes equations bring out a new challenge to solve which is Reynolds stress term [7]. Boussinesq hypothesis is one of the ideas representing that turbulent eddies can be calculated with the assumption of eddy viscosity formulation [8]. In this case, turbulence models differ from the turbulent eddy viscosity assumption in the Reynolds stress tensor. Such models like algebraic, one equation, two equation etc. are derived to represent the effect of the turbulence [9]. In this context, some of the numerical applications are based on the Spalart-Allmaras found in literature. At the same time, the existence of several studies using k-ϵ and k-ω turbulence solvers has been observed [10] [11] for nacelle shape. The difference between the turbulence models and detailed information about each one is presented in the coming sections.

1.1.2.3 Optimization Methods

The optimization implies the whole process of the modifications that are performed on any mechanism or system to get closer to the desired parametric data. With the development of computer and software technologies, dozens of different innovative optimization techniques have taken their place today. In shape optimization cases, the main goal is to reach the optimal shape from baseline model according to desired outputs by assigning some constraints. Some of the optimization techniques used in different papers are briefly explained below.

Gradient optimization is a technique used in machine learning and other fields to find the parameters of a model that minimize a loss function. The loss function is the measure of how well the model fits the parametric data. Gradient optimization works by iteratively updating the parameters of the model in the direction of the steepest descent of the loss function [12]. This means that the parameters are updated in the direction that will most quickly reduce the value of the loss function. The direction of the gradient-based optimization is affected by the starting point and first order iterative progression of the problem where the objective function gets multiple local optimal points [13].

Stochastic optimization, also known as random optimization, is a type of optimization algorithm that incorporates randomness into the search process [14]. This randomness can be used to escape local optima and find better solutions in high-dimensional spaces.

Surrogate models, also known as metamodels, are type of statistical model recently used to estimate the behavior of a computationally expensive simulation or optimization problem [15]. This model is kind of a machine learning where the surrogate model can be used to learn the relationship between the input parameters and results without calculating the actual function or model [16]. It could be introduced as statistical model to approach the solution. This can be useful for tasks such as hyperparameter optimization or model selection, where evaluating the full

model is time-consuming or expensive [17]. One of the common types of surrogate model is a Gaussian process (GP) which is a Bayesian model using a normal distribution to represents the posterior distribution over the approximated function [18]. Moreover, GPs are generally well-suited for surrogate modeling because they can capture complex relationships between input features and outputs and can be updated efficiently as new data becomes available.

The Multi-Objective Genetic Algorithm (MOGA) was developed by John Holland in the 1970s [19]. which is a search heuristic that is used to solve complex optimization problems with multiple objectives. MOGA is a type of evolutionary algorithm that is inspired by the process of natural selection [20]. MOGAs are particularly well-suited for problems where the objectives are conflicting, meaning that there is no single solution that can optimize all the objectives simultaneously [21]. Also, this algorithm is embedded in the commercial flow solver Ansys program which allows scientists to study new research topics and experiments in recent years [22] [23]. Even if this algorithm is a powerful tool for computing complex optimization problems over given bodies, it can also be computationally expensive. Moreover, MOGA is used to find a set of Pareto optimal which is a type of evolutionary algorithm that is inspired by the process of natural selection [24]. MOGA works by iteratively updating a population of candidate solutions. Each candidate solution is evaluated based on its performance with respect to input and desired objectives. After that, the best-performing solutions are selected and recombined to create new candidates. This process is repeated until a satisfactory set of Pareto optimal solutions are found.

1.2 Objective and Scope of Thesis

The objective of the thesis is to optimize a given baseline turbofan nacelle inlet shape and improve its aerodynamic performance by applying Multi-Objective Genetic Algorithm (MOGA) technique in conjunction with provided flow solutions from a commercial computational flow solver. In order to reduce the computational

time, Pareto optimal solutions are used which is a concept used in optimization theory that describes a set of solutions where no solution can be improved in any objective without worsening another objective.

The baseline nacelle shape is taken from literature, and parametric design points are assigned on the shape. The optimization is then carried out over these points with a defined objective function. The objective function is defined based on weighted sum of increasing the flow pressure recovery ratio by the fan area and decreasing the nacelle drag coefficient. Two different independent operating points are considered for optimization. These are cruise and take-off conditions. As by product of the optimization procedure, the relationship between the different optimization parameters assigned to the design are observed. Finally, the desired values specified in the objective function for the baseline model and optimized shape given by Pareto optimal are compared.

1.3 Outline of Thesis

In Chapter 1, brief information on nacelle designs and their aerodynamic performance is provided. Then, main problems faced and breakthroughs to their solutions are addressed. Then, numerical approaches to solution of nacelle design in different flight conditions are explained with brief information on optimization techniques. Finally, the aims, solution-optimization techniques and the results found in similar literature studies are explained briefly.

Chapter 2 provides the detailed information of the formulation on Navier-Stokes equations and governing equations. Moreover, this section includes the different methodologies used in turbulent flow simulations. Then, the details of performance parameters are provided.

Validation study is carried out and some useful charts and figures are given and described in Chapter 3. After the validation study, analysis is carried out under a different condition.

Chapter 4 includes the outcomes of the Multi-Objective Genetic Algorithm (MOGA). Also, this section shows the initial samples with cross validation, comparison of each sample, trade-off results between output parameters which are bounded to the objective and penalty function. Moreover, validations of results are shown with related graphs, tables, and figures.

Chapter 5 provides the conclusion section of the thesis with gains and outcomes based on MOGA, and includes the comments made based on these results.

CHAPTER 2

METHODOLOGY

Numerical flow solutions that are required by the optimization stage are obtained by solving the Reynolds-Averaged Navier-Stokes (RANS) equations with a turbulence model. Geometric design optimizations that utilize these solutions are carried out using a Multi Objective Genetic Algorithm (MOGA) method. In this section, the numerical flow solver with the employed turbulence models is described first. Then, the Multi-Objective Genetic Method (MOGA) is explained in detail. This is followed by an introduction of the baseline nacelle geometry, and description of the meshing and numerical flow solution strategy. Shape optimization procedure is also explained in this chapter. Moreover, priorities of parameters calculated in optimization technique are introduced with related formulations, and definition of the objective function used in MOGA optimization.

2.1 Overall Approach

In this section, the required tools for the design process, CFD analysis and the optimization are introduced. Afterwards, the details of how these tools exchange data with each other and how they operate sequentially are given. The main tools used in this thesis study could be grouped into three main groups which are DesignModeler, computational flow solver and optimizer, which are all embedded on Ansys Workbench.

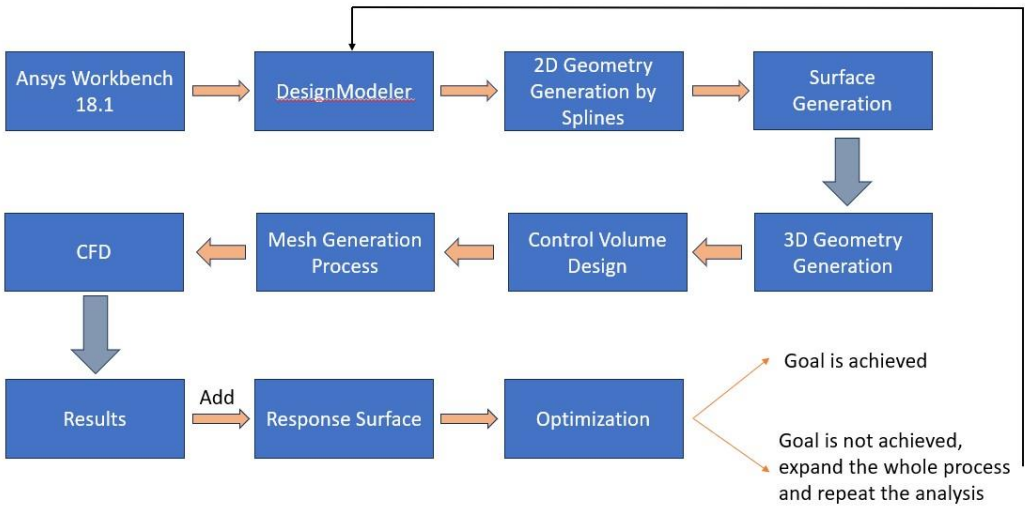

Figure 2.1. Overall Approach Scheme

The order of operation and the relationship of the tools are schematized detailly in Figure 2.1. First, the nacelle geometry creation is performed using the DesignModeler tool, which is embedded in ANSYS Workbench. In this part, the points that define the nacelle geometry are formed and these points are united with splines. While designing the nacelle shape, a reference coordinate system is defined and the whole procedure adheres to that. The baseline geometry is an axisymmetric turbofan geometry, as taken from a reference study. The points that define this shape are available only from the lip of the inlet to the fan. Outside part of the inlet shape is fitted by a NACA curve for convenience. Then, the formed two-dimensional (2D) shape is revolved about the axis of the engine to form the three-dimensional (3D) geometry.

After the generation of 3D model, the flow solution domain is created. The outer boundary of the flow domain is drawn as a conical shape, with increasing radius downstream to make sure the side surface of this shape acts as a far-field flow inlet boundary. Then, the computational flow mesh is generated. In the meshing process, the aim is to divide the control volume into smaller cells at which flow conservation equations are applied, and the resulting algebraic equations are solved.

Flow solutions are obtained by the commercial computational fluid dynamics (CFD) solver Fluent. The case file of the control volume including meshes are submitted to the Fluent solver to obtain the solution. After the flow analysis on the baseline model, an additional matrix of 80 unique nacelle shapes with defined distortions to the baseline geometry is created to form the response surface with the same boundary conditions and flow solution parameters. The response surface in Ansys Fluent is a mathematical model used to predict the effect of a set of design variables on the output variables. The purpose of doing this is to examine the effects of variations of geometric design points on the objectives and create a preliminary idea for optimization.

The constructed response surface is then utilized in an optimizer. In this study, a Multi-Objective Genetic Algorithm (MOGA) is employed. The connection between the response surface and MOGA is that the response surface provides MOGA with a starting point to find optimal design points for desired outputs. The response surface estimates the relationship between design variables and the response variable. Then, MOGA tries to find the most optimum points by using the predictions of response surface.

Finally, the suggested points by MOGA are tested by a Fluent analysis for verification. If the output estimated at the design points suggested by MOGA are close to the results obtained from the flow analysis, the algorithm is said to have worked properly and an optimized shape has been produced. Otherwise, the process is repeated from the beginning of the entire procedure, from the DesignModeler tab to the final flow analysis performed as the last step for checking the optimization result. The whole procedure is summarized in Figure 2.1.

2.2 Flow Computations

For the computational fluid dynamics part of the study, the commercial solver Fluent v18.1 is employed. Fluent uses the finite volume method (FVM). The basic principle of FVM is to discretize the governing into small non-overlapping control volumes, called finite volumes. Then, the same conservation equations are applied to each constituent element of the whole computational domain linking the discrete solutions across the domain. Various discretization schemes are available in Fluent. In this study, the schemes based on implicit formulation are used with density-based formulation [74]. Implicit formulations are more stable allowing larger time steps for accelerated convergence toward steady-state solutions.

The solved flow equations are the Reynolds-Averaged Navier Stokes equations (RANS). A turbulence model is required for closing these equations. Common RANS turbulence models used in Fluent are k-ε, k-ω and Spalart-Allmaras model. The solutions provided by these turbulence models for the baseline geometry will be evaluated later in this chapter. The most cost effective accurate enough turbulence model will be selected for the shape optimization study.

All in all, the governing equations of fluid flow are converted into algebraic equations which are discretized in next step using a finite volume method in Fluent. Then, these algebraic equations are linearized. After that, the solution is provided within this way until the convergence is achieved.

2.2.1 Governing Equations

The mathematical description of the problem which generates the main framework of the computational algorithm are referred to as governing equations. In this manner, suitable for flows are the conservation of mass, momentum, and energy equations.

The conservation of mass equation is given by,

$$\frac{\partial \rho}{\partial t} + \frac{\partial (\rho u_i)}{\partial x_i} = 0 \tag{2.1}$$

where ρ is the density of the fluid flow and u_i is the velocity in x, y and z directions.

This equation is also known as the conservation of mass, ensures that mass is conserved within a fluid flow. It ensures that the rate of change of mass in a given control volume needs to be equal the net mass flux into or out of the control volume.

The conservation of momentum equation is given by,

$$\frac{\partial (\rho u_i)}{\partial t} + u_j \frac{\partial (\rho v_i)}{\partial x_j} = -\frac{\partial P}{\partial x_i} + \frac{\partial \tau_{ij}}{\partial x_j} + \rho g_i \tag{2.2}$$

where P is the pressure, τ_{ij} is the shear stress of the fluid flow and g_i is the gravity.

The Navier-Stokes equations describe the conservation of momentum for fluid flow. This equation includes three equations: one for each component of velocity (x, y, and z). These equations consider the effects of pressure, viscous forces, and the convective acceleration of the fluid.

Since the Newtonian assumption states that the viscosity is not affected by shear rate, the stress tensor formulated as follows.

$$\tau_{ij} = 2\mu S_{ij} + \lambda \frac{\partial v_k}{\partial x_j} \delta_{ij} \tag{2.3}$$

where δ_{ij}, μ and λ represents the Kronecker delta, viscosity of the fluid flow and kinematic viscosity of the flow respectively. In shear stress term, Sutherland's law is used for dynamic viscosity term μ to observe the effects of temperature on dynamic viscosity.

$$\frac{\mu}{\mu_{ref}} = \left(\frac{T}{T_{ref}}\right)^{\frac{3}{2}} \frac{T_{ref} + S}{T + S} \tag{2.4}$$

where T_{ref} is the reference temperature, μ_{ref} is the reference viscosity at the given T_{ref} and S is the Sutherland temperature. Also, this formula could be interpreted as below.

$$\mu = \frac{C_1 T^{\frac{3}{2}}}{T + S} \tag{2.5}$$

Comparing the formulas above, C_1 constant can be written as below.

$$C_1 = \frac{\mu_{ref}}{T_{ref}^{\frac{3}{2}}} \left(T_{ref} + S\right) \tag{2.6}$$

Moreover, these coefficients used in Sutherland's law are given at table below.

Table 2.1. Sutherland's Law Coefficients

Gas	$\mu_0 \left[\frac{kg}{ms}\right]$	$T_0[K]$	$S[K]$	$C_1 \left[\frac{kg}{ms\sqrt{K}}\right]$
Air	1.716×10^{-5}	273.15	110.4	1.458×10^{-6}

All in all, this formula can be transformed into formula given below.

$$\mu = \mu_0 \frac{T^{\frac{3}{2}}}{T + 110.4} \tag{2.7}$$

where μ_0 is given above in table 2.1.

Then, the thermal energy conservation equation is given where the right-hand side of the equation includes all the force terms such as shear, surface, and body forces.

$$\frac{\partial(\rho h)}{\partial t} + \frac{\partial(\rho h u_i)}{\partial x_i} = \frac{\partial}{\partial x_i}\left(k \frac{\partial T}{\partial x_i}\right) + S \tag{2.8}$$

where k denotes thermal conductivity coefficient, h represents total enthalpy and S represents the heat dissipation term.

The energy equation is used to analyze temperature and thermal energy transport within a fluid. It includes terms for conduction, convection, and the generation or dissipation of energy within the fluid flow.

Furthermore, the Navier-Stokes equations are interconnected and must be solved concurrently. In the case of three-dimensional compressible analysis, there are 6 flow variables to be computed, whereas the Navier-Stokes equations consist of 5 conservation equations. As a result of the compressibility of the flow, the pressure is determined using the perfect gas assumption, which allows the equation of state to close the system.

$$P = \rho RT \tag{2.9}$$

where ρ, R and T are the density, gas constant and the static temperature of the given fluid flow respectively.

2.2.2 Turbulence Models

The Reynolds-Averaged Navier-Stokes (RANS) equations provide a middle ground by averaging the time dependent conservations equations given above over time to incorporate turbulence effects without explicitly computing and solving each eddy and fluctuation. The resulting time-averaged equations are closed by a suitable turbulence model (turbulence transport equation) for the resulting Reynolds stresses due to time averaging [42]. RANS equations are commonly closed using the k-ε model, k-ω model, the Reynolds stress model (RSM), and the Spalart-Allmaras model, among others. Each model has specific assumptions and uses different approach to solve the turbulent flow problems.

In RANS equations, flow parameters are splitted into average and fluctuation components such as the for the *x*-direction, *x*-velocity is decomposed into $\bar{u}$ and

u'which represents average velocity and fluctuation velocity respectively. In averaged momentum equations, terms such as $\rho\overline{u'v'}$ appears because of Reynolds decompositions in Navier-Stokes equations. Eddy viscosity concept inside the turbulence is responsible for these terms.

In RANS equations, flow parameters are splitted into average and fluctuation components such as the for the *x*-direction, *x*-velocity is decomposed into $\bar{u}$ and u'which represents average velocity and fluctuation velocity respectively. In averaged momentum equations, terms such as $\rho\overline{u'v'}$ appears because of Reynolds decompositions in Navier-Stokes equations. Eddy viscosity concept inside the turbulence is responsible for these terms.

$$\tau_{ij}^{R} = -\rho\overline{u'v'} = 2\mu_T\overline{S_{ij}} - \frac{2}{3}\rho K\delta_{ij} \tag{2.10}$$

where δ_{ij} and K represent the Reynolds-Averaged strain rate tensor and turbulent kinetic energy respectively. However, there is a closure problem for the RANS equations with these additional terms because of the altercation of fluctuating parts inside the number of equations. In order to satisfy this problem, the Boussinesq hypothesis [43] is used to model the turbulent problem. The Boussinesq hypothesis is frequently used in many problems such as natural convection, where temperature gradients lead to variations in fluid density. It simplifies the governing equations (such as the Navier-Stokes and energy equations) and allows for the study of buoyancy-driven flows without the need to track density variations explicitly. Also, Boussinesq assumption includes the idea of extra dissipation term that is created by turbulent stresses. However, it should be noted that the the Boussinesq hypothesis might not be accurate for simulations with large variations in density or high-speed compressible flows. The linear eddy viscosity models are divided into such groups given below.

- Algebraic Models
- One Equation Model (Spalart-Allmaras Model, Prandtl's Model, etc.)
- Two Equation Model (Realizable *k*-ϵ, SST *k*-ω, etc.)

In this thesis, Spalart Allmaras which is one-equation turbulence model is used to investigate the fluid flow in given nacelle shape.

2.2.2.1 Spalart-Allmaras Turbulence Model

The Spalart-Allmaras turbulence model is a Reynolds-Averaged Navier Stokes equation approach including a single governing kinematic equation to identify the viscous eddies *v* in flow. Especially, this one equation model is derived to be used in aerodynamic problems including wall-bounded systems. So many parameters and coefficients are included in this approach but since there is only one dynamic differential equation to solve, this turbulence model requires less time than other turbulence models such as Realizable *k-ϵ*, SST *k-ω*, etc. Some of the advantages of this model are indicated below.

- Lower complexity
- Less overall simulation time
- Useful for boundary layer flows with arbitrary pressure gradients

However, this model has some limitations because of unreliability to identify decay of turbulent flows. Moreover, the efficiency of this model beyond wall-bounded systems is still suspicious. Therefore, the researchers still try to investigate this model to better understandings in turbulent flow behavior and computing.

The one equation Spalart-Allmaras turbulence model formulation [44] given in tensor notation as below.

$$\begin{aligned}\frac{\partial \bar{v}}{\partial t} + u_j \frac{\partial \bar{v}}{\partial x_j} &= C_{b1}(1 - f_{t2})\bar{S}\bar{v} \\ &+ \frac{1}{\sigma}\left\{\frac{\partial}{\partial x}\left[(\nu_L + \nu)\frac{\partial \bar{v}}{\partial x_j}\right] + C_{b2}\frac{\partial \bar{v}}{\partial x_j}\frac{\partial \bar{v}}{\partial x_j}\right\} \\ &- \left[C_{w1}f_w - \frac{C_{b1}}{\kappa^2}f_{t2}\right]\left(\frac{\bar{v}}{d}\right)^2 + f_{t1}\|\Delta\vec{u}\|_2^2\end{aligned} \quad (2.11)$$

The eddy viscosity production terms are given below.

$$\bar{S} = f_{v3}S + \frac{\bar{u}}{\kappa^2 d^2} f_{v2} \tag{2.12}$$

where S represents the magnitude of the mean rotation rate.

$$f_{v1} = \frac{\chi^3}{\chi^3 + {C_{v1}}^3}, \quad f_{v2} = \left(1 + \frac{\chi}{C_{v1}}\right)^{-3} \tag{2.13}$$

$$f_{v3} = \frac{(1 + \chi f_{v1})(1 - f_{v2})}{\max(\chi, 0.001)}, \quad \chi = \frac{\bar{\nu}}{\nu} \tag{2.14}$$

$$S = \sqrt{2\Omega_{ij}\Omega_{ij}} \tag{2.15}$$

The laminar-turbulent transition terms are written as

$$f_{t1} = C_{t1} g_t \exp\left(-C_{t2} \frac{w_t^2}{\Delta U^2}(d^2 + g_t^2 d_t^2)\right) \tag{2.16}$$

$$f_{t1} = C_{t3} \exp(-C_{t4}\chi^2), \quad g_t = min\left[0.1, \frac{\left\|\overrightarrow{\Delta u}\right\|_2}{w_t \Delta x_t}\right] \tag{2.17}$$

where w_t, $\overrightarrow{\Delta u_2}$, d_t, Δx_t represents the vorticity at the wall at the trip point, two-norm of difference between velocity at the trip and current field section, the distance to the nearest trip point and the spacing along the trip point, respectively.

All in all, the constant parameters in one equation turbulence model of Spalart-Allmaras are given below.

$$C_{b1} = 0.1355, \quad C_{b2} = 0.622, \quad C_{v1} = 7.1, \quad C_{v2} = 5$$

$$\sigma = \frac{2}{3}, \quad \kappa = 0.41,$$

$$C_{w1} = \frac{C_{b1}}{\kappa^2 + \frac{(1 + C_{b2})}{\sigma}}, \quad C_{w2} = 0.3, \quad C_{w3} = 2$$

$$C_{t1} = 1, \quad C_{t2} = 2, \quad C_{t3} = 1.3, \quad C_{t4} = 0.5$$

2.2.2.2 Realizable *k-ϵ* Turbulence Model

The standard form of *k-ϵ* model is a two-equation empirical model where the solution of two separate transport equations independent determination of turbulent velocity and length scales. The standard *k-ϵ* model used in CFD problems become a huge touchstone in flow simulations since it was proposed by Launder and Spalding [45]. The *k* and *ϵ* that give the equation its name represents the turbulent kinetic energy and dissipation rate respectively. In the standard *k-ϵ* model, it is assumed that the flow is fully turbulent, and this is the weakness of this model since the effects of molecular viscosity are negligible. Since, the standard *k-ϵ* model is inefficient for flows with adverse pressure gradients, improvements have been made for this model and it is called as realizable *k-ϵ* which was introduced by Shih [46]. The model is named as realizable because the model satisfies special constraints on Reynolds stresses and plausible with the physics of turbulent flows. The main difference between the models could be interpreted as to provide more accurate predictions near solid walls, where the standard k-ε model tends to struggle because realizable model captures the near-wall turbulence behavior better with wall-bounded effects [47]. In formulation, the main difference between the models comes from the eddy-viscosity explanation and the derivation of the mean square vorticity fluctuations.

The transport equations for realizable *k-ϵ* model are given by.

$$\frac{\partial}{\partial t}(\rho k) + \frac{\partial}{\partial x_j}(\rho k u_j) = \frac{\partial}{\partial x_j}\left[\left(\mu + \frac{\mu_t}{\sigma_k}\right)\frac{\partial k}{\partial x_j}\right] + G_k + G_b - \rho\epsilon - Y_M + S_k \quad (2.18)$$

$$\frac{\partial}{\partial t}(\rho\epsilon) + \frac{\partial}{\partial x_j}(\rho\epsilon u_j) = \frac{\partial}{\partial x_j}\left[\left(\mu + \frac{\mu_t}{\sigma_\epsilon}\right)\frac{\partial \epsilon}{\partial x_j}\right] + \rho C_1 S\epsilon - \rho C_2 \frac{\epsilon^2}{k + \sqrt{\nu\epsilon}} + C_{1\epsilon}\frac{\epsilon}{k}C_{1\epsilon}G_b + S_\epsilon \quad (2.19)$$

where the coefficients are,

$$C_1 = max\left[0.43, \frac{\eta}{\eta+5}\right], \quad \eta = S\frac{k}{\epsilon}, \quad S = \sqrt{2S_{ij}S_{ij}}$$

For improvements, C_μ is not constant as in standard $k-\epsilon$ turbulence model. So new C_μ formulation is given below.

$$C_\mu = \frac{1}{A_0 + A_S\frac{kU^*}{\epsilon}} \tag{2.20}$$

A_0 and A_s are the coefficients of the given model.

$$A_0 = 4.04, \quad A_s = \sqrt{6}\cos(\phi) \tag{2.21}$$

where

$$\begin{aligned} \phi &= \frac{1}{3}\arccos\left(\sqrt{6}W\right) \\ W &= \frac{S_{ij}S_{jk}S_{ki}}{\widetilde{S^3}} \\ \tilde{S} &= \sqrt{S_{ij}S_{ij}} \\ S_{ij} &= \frac{1}{2}\left(\frac{\partial u_j}{\partial x_i} + \frac{\partial u_i}{\partial x_j}\right) \end{aligned} \tag{2.22}$$

where U^* is another parameter here and formulation of U^* is given below.

$$U^* = \sqrt{S_{ij}S_{ij} + \widetilde{\Omega}_{ij}\widetilde{\Omega}_{ij}} \tag{2.23}$$

Also, there is new coefficients in U^* and they are introduced below.

$$\widetilde{\Omega}_{ij} = \Omega_{ij} - 2\epsilon_{ijk}\omega_k \tag{2.24}$$

$$\Omega_{ij} = \overline{\Omega}_{ij} - \epsilon_{ijk}\omega_k \tag{2.25}$$

$\overline{\Omega}_{ij}$ in the equation given above represents the mean rotation rate tensor that is viewed in a rotating frame with the angular velocity which is represented by ω_k.

2.2.2.3 SST $k-\omega$ Turbulence Model

The SST $k-\omega$ (Shear-Stress Transport) turbulence model is a two equation and hybrid turbulence model that combines the basis of the standard $k-\omega$ and $k-\epsilon$ turbulence models. In the name of equation, k and ω represents turbulent kinetic energy and specific rate of dissipation. This model is widely used in various applications, especially in topics related to fluid dynamics and aerodynamics. The SST $k-\omega$ is aims to perform better in such cases where flow separation occurs. Moreover, this model aims to provide more accurate predictions in near-wall regions and free shear layers. The SST $k-\omega$ model is found and formulated by Menter [48] in order to solve the flow behavior at the inner part of boundary layer. The standard form of $k-\omega$ is convenient for flows which have lower Reynolds number where viscous terms are dominant. However, the SST $k-\omega$ model ensures better performances in predicting separated flows, recirculation, complex geometries at higher Reynolds number where the inertial forces are dominant. One such missing thing for SST model is that lower prediction capability at where higher velocity gradients occur.

The kinematic eddy viscosity ν_T, turbulence kinetic energy (k) and specific dissipation rate (ω) formulations taking part in SST $k-\omega$ model is given below respectively [49].

$$\nu_T = \frac{a_1 k}{\max(a_1\omega, SF_2)} \tag{2.26}$$

$$\frac{\partial k}{\partial t} + U_j\frac{\partial k}{\partial x_j} = P_k - \beta^* k\omega + \frac{\partial}{\partial x_j}\left[(\nu + \sigma_k\nu_T)\frac{\partial k}{\partial x_j}\right] \tag{2.27}$$

$$\frac{\partial \omega}{\partial t} + U_j\frac{\partial \omega}{\partial x_j} = \alpha S^2 - \beta\omega^2 + \frac{\partial}{\partial x_j}\left[(\nu + \sigma_\omega\nu_T)\frac{\partial \omega}{\partial x_j}\right] + 2(1-F)\sigma_{\omega 2}\frac{1}{\omega}\frac{\partial k}{\partial x_i}\frac{\partial \omega}{\partial x_i} \tag{2.28}$$

where the coefficients are given as

$$\sigma_{\omega 1} = 0.5, \quad \sigma_{\omega 2} = 0.856, \quad \beta^* = \frac{9}{100} \tag{2.29}$$

Moreover, the governing equation for this model is written as below.

$$\frac{\partial(\rho k)}{\partial t} + \frac{\partial(\rho k u_i)}{\partial x_i} = \frac{\partial}{\partial x_i}\left(\Gamma_k \frac{\partial k}{\partial x_j}\right) + \tilde{G}_k - Y_k + S_k \tag{2.30}$$

$$\frac{\partial(\rho \omega)}{\partial t} + \frac{\partial(\rho \omega u_i)}{\partial x_i} = \frac{\partial}{\partial x_j}\left(\Gamma_\omega \frac{\partial}{\partial x_j}\right) + G_\omega - Y_\omega + S_\omega + D_\omega \tag{2.31}$$

where $\tilde{G}_k$ represents the turbulence kinetic energy generation by mean velocity gradients, G_ω shows the specific rate of dissipation, Γ is the effective diffusivity, Y represents the dissipation of turbulence, D_ω represents the cross diffusion and lastly S is defined as the source.

2.2.2.4 Isentropic Relations

In the analysis section, since the density-based solver is selected, the isentropic relations should be computed for both pressure and temperature. In isentropic relation formulas, the relationship between variables in a process where the entropy of the gas remains constant is defined. These formulas help us to understand how gases behave in compressors, turbines, and other gas fluid devices. The formulas used in the isentropic relations to compute the related pressure and temperature for the boundary condition implementation is given below [50].

$$\frac{P_0}{P} = \left[1 + \left(\frac{\gamma - 1}{2}\right) M^2\right]^{\frac{\gamma - 1}{\gamma}} \tag{2.32}$$

$$\frac{T_0}{T} = 1 + \left(\frac{\gamma - 1}{2}\right) M^2 \tag{2.33}$$

where P_0 is the total pressure, P is the static pressure, γ is air constant, M is Mach number, T_0 and T represent the total pressure and static pressure, respectively.

2.2.3 Geometry Description

The geometry optimized in the work is the air inlet part of a nacelle that houses a turbofan engine powering a mid-to-long-range aircraft [51]. The points defining the geometry are extracted from the work of [52]. In the optimization framework, first the extracted points are entered one by one into the DesignModeler tool. These points are considered as the design points and are shown in Figure 2.2. Then, these design points are combined with a spline method to obtain a 2D shape. While doing this, the connections between the design points, such as the slope between some points being zero, are taken into consideration.

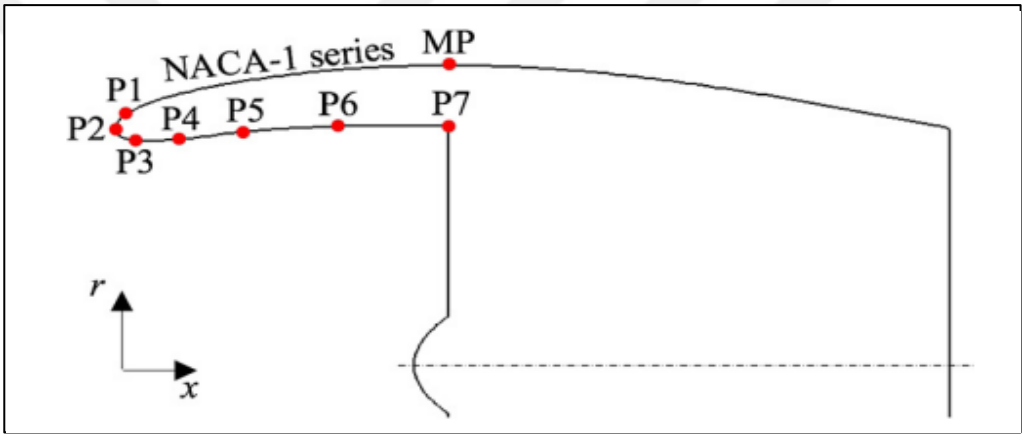

Figure 2.2. Geometry Parameters of Nacelle Shape [52]

The numerical values of the design points (P) are given in Table 2.2. The points P2, P3, P4, P5 are set as the active points in the design. That is, they are the points allowed to move during the optimization. The rest of the points are specified as fixed. While both horizontal and radial displacements are allowed for points P3, P4 and P5, only radial displacement is allowed for P2. This way the length of the inlet as well as the fan radius is kept unchanged with respect to the baseline geometry.

Table 2.2. Lower and Upper Bounds of Control Points (m)

Points	***Baseline (x,r)***	***x-Coordinate***	***r-Coordinate***
P1	*(0.0078, 0.8008)*	*Fixed*	*Fixed*
P2	*(0, 0.7756)*	*Fixed*	*0.76-0.78*
P3	*(0.1459, 0.7369)*	*0.12-0.18*	*0.73-0.76*
P4	*(0.3264, 0.7575)*	*0.30-0.35*	*0.75-0.79*
P5	*(0.5018, 0.7744)*	*0.48-0.52*	*0.76-0.78*
P6	*(0.6927, 0.7839)*	*Fixed*	*Fixed*
P7	*(1.0000, 0.7861)*	*Fixed*	*Fixed*

The coordinate details of the shape should be well defined to create a smooth design of the nacelle. This is done using splines. There exist several spline methods that are commonly used to define the surfaces. These spline methods are important for defining the shapes of components of aircrafts including wings, fuselages, nacelle as well as for solving various design and analysis problems. In this thesis, Bezier splines are used which is explained below.

B-splines are widely used in aerospace engineering for defining complex curves and surfaces. They are a generalization of Bezier curves and offer greater flexibility in shaping curves [53]. B-splines are often used in CAD/CAM (Computer-Aided Design and Computer-Aided Manufacturing) and finite element analysis (FEA) for modeling and simulating aerospace components.

Bezier spline method, which is a type of mathematical curve used in various fields is selected to create the two-dimensional nacelle shape first. The theory behind the Bezier curve is that it is a parametric curve defined by a set of control points.

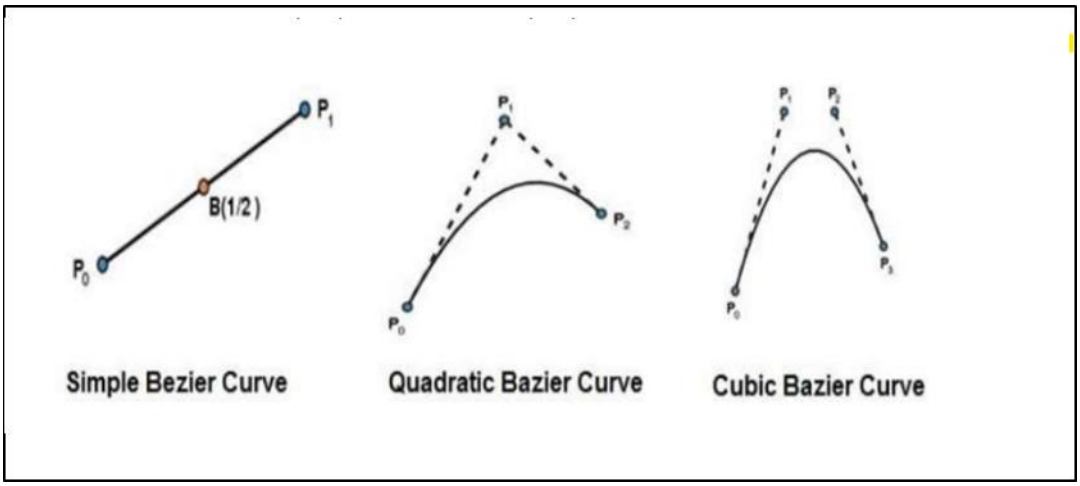

Figure 2.3. Common Bezier Curves [54]

Simple Bezier Curve and Quadratic Bezier Curve are kind a simple relative to the Cubic Bezier Curve because it contains 2 and 3 control points respectively. However, more complex curves, cubic Bezier curves are used. They are defined by four control points.

$$P(t) = \sum_{i=0}^{b} B_i^n(t).P_i t \in [0,1] \qquad (2.34)$$

where, *B(t)*, Bernstein polynomial given as.

$$B(t) = (1-t)^3.P_0 + 3.(1-t)^2.t.P_1 + 3.(1-t).t^2.P_2 + t^3.P_3 \qquad (2.35)$$

where P_0, P_1, P_2, P_3 are control points. P_0 is the start point, P_3 is the end point, and P_1 and P_2 influence the curvature of the curve.

2.3 Optimization Methodology

This section explains the importance of the optimization and the basic optimization techniques used in the design of the inlet geometry in this thesis. Optimization is such a process that includes calculating and finding the best optimal solution or some sort of parameters to achieve a specific goal or objective while sticking a set

of constraints. The optimization of the nacelle inlet refers to the process of improving the design and configuration of the nacelle [55].

There are several reasons to optimize nacelle inlet. First of all, pressure recovery ratio on the fan area should be as high as possible which could improve the overall engine efficiency because the less pressure drop occurs, the higher the engine efficiency. Another important is to check is that the uniformity of flow coming into fan area. The disturbances of flow in both radial and azimuthal direction should be kept at minimum levels for smooth distribution of pressure on fan area. Also, the nacelle body produces a drag force like other segments of the aircraft and reducing this force is important in terms of fuel consumption. Moreover, inlet optimization could reduce the maximum Mach number observed on the nacelle surface. This is also important because as the speed of flow approaches to higher Mach numbers, the skin coefficient and temperature of the surface could increase which might reduce the engine efficiency. All in all, the inlet optimization on nacelle is performed to increase the pressure recovery ratio on the fan, reduce the drag coefficient of the nacelle body, reducing the maximum Mach number on the body and increase both the smoothness and uniformity of the flow approaching to fan. Also, there is another common objective in inlet shape optimization which could attempt to reduce noise levels by changing the geometrical shape.

Overall, nacelle inlet optimization is essential for achieving a balance between aerodynamic efficiency, engine performance and other key factors in aircraft design.

In this thesis, although there are many different objectives in inlet optimization, only the pressure recovery ratio at the fan surface and drag coefficient value are tried to be optimized, since numerical solution times are also taken into account. The optimization procedure is explained in the following subheadings.

2.3.1 Response Surface Method

Response Surface Method (RSM) is a widely used optimization method which employs a statistical model approach to figure out the relationship between input parameters and the desired output or response of the analysis. RSM is typically a polynomial function gathering the behavior of the output variables within a limited range of the inputs.

RSM is implemented in modules of Ansys, including DesignModeler and Fluent. It is generally useful for optimization stage of complex problems where evaluating the objective function is computationally expensive or time-consuming. By utilizing a surrogate model, RSM can efficiently explore the design space and identify promising regions without requiring excessive simulations or experiments [60].

In this thesis, a RSM is used in Ansys Workbench which is an appropriate starting point for optimization algorithm. The stages of the response surface are starting with the preliminary design, also called as design of experiments, in where a matrix of values including the design variables is created. This matrix determines the range of design variables and how many different values to use for each variable. Then, a response surface is created using this matrix. The response surface is used to estimate the effect of each design variable on outputs which are pressure recovery ratio and drag coefficient. Then, these results are sent to the MOGA which is explained further detail in following chapters.

2.3.1.1 Parameters of Correlation

In Ansys Response Surface, the parameters of correlation section give useful preliminary information into the relationships between the input design parameters and the response variable. These relations between parameters give understanding in the sensitivity of the response to changes in the input variables and identify potential interactions and relations between them.

2.3.1.2 Correlation Matrix

The correlation matrix represents the degree of linear association between each determined input parameters which is written in a square matrix form where each element (r_{ij}) represents the correlation coefficient between the input variables between each direction which are represented as i and j. As values between initial parameters getting close to 1, strong positive correlation takes place. Within the same manner, as values getting close to -1, a strong negative correlation takes place. However, values close to 0 indicate that there is a weak or no correlation between design points. The formulation of the correlation matrix is shown below.

$$r_{ij} = \frac{cov(x_i, x_j)}{\sigma_i \sigma_j} \tag{2.36}$$

where $cov(x_i, x_j)$ represents the covariance between input variables, $\sigma_i$and σ_j represent the standard deviation of x_i and x_j respectively.

2.3.1.3 Sensitivities

In RSM, the sensitivities section calculates the relative change in the response variables for a unit change in each input design parameter. Moreover, this calculation shows the degree to parameters which the response is affected by changes in the inputs. Higher sensitivity implies that the corresponding input variable has a greater influence on the response.

$$Sensitivity\ of\ Response\ to\ Input\ Variable\ i = \frac{\partial y}{\partial x_i} \tag{2.37}$$

where $\frac{\partial y}{\partial x_i}$ is the partial derivative of the response y with respect to input variable x.

2.3.1.4 Determination Matrix

The determination matrix which also known as the R-squared matrix provides a measure of the goodness of fit of the given response surface model [61]. Determination matrix represents the proportion of the variation in the response variable that can be explained by the input variables. Better fit of the given model is ascertained with higher determination coefficients (R^2). The formulation of determination coefficients is found as following formula.

$$R^2 = 1 - \frac{SSR}{SST} \tag{2.38}$$

where SSR is the sum of squared residual and SST is the total sum of the squares.

2.3.1.5 Correlation Scatter

Correlation scatter is the plotting section of the representation scheme of the correlation between each input design parameters. This representation scheme displays the data points along with a trendline which allows for identification correlations whether it is strong or weak. [62]. This graphic of correlation has an important meaning in understanding the behavior of the response surface along the RSM. After analyzing these input parameters, the most influential input variables could be identified. Also, potential interactions between variables could be checked to gain more efficient design model.

2.3.1.6 Cross Validation

Cross validation is used in RSM which is used to validate the model by extracting the limited data to be compared. The given models are tested and compared with the data that are not available in process which assesses how well the response surface model generalizes to unseen data. Then, cross validation checks and estimates the error of each data in each model [63].

Moreover, the cross-validation (schematically shown in Figure 2.4) is a useful tool to improve the reliability of response surface models. By incorporating cross-validation into the process, optimized design models could be achieved accurately.

Figure 2.4. Diagram of the 5-Fold Cross-Validation Method [64]

This figure given above shows the cross-validation model. For each model, each indicator number is tested, and errors are fold. The total error can be used as an objective function in the optimization algorithm. By minimizing the total error, the aim of the optimization algorithm is to find a model for unknown data sets. The formulation is represented below.

$$E = \frac{1}{k}\sum_{i=1}^{k} E_i \tag{2.39}$$

where k is the number of the folds, and E_i is the error for each data.

2.3.2 Multi-Objective Genetic Algorithm

Ansys Workbench provides tools and algorithms for performing optimization experiments. Common optimization algorithms used in CFD may include genetic algorithms, gradient-based methods, and surrogate modeling techniques.

In the optimization methodology, a Multi-Objective Genetic Algorithm (MOGA) with Kriging interpolation is used which generates optimal solutions for multi objective problems. One of the advantages of MOGA is the ability to explore different solutions in the design space and to provide more comprehensive and varied results based on genetic algorithm principles. The working sequence of MOGA is shown in Figure 2.5.

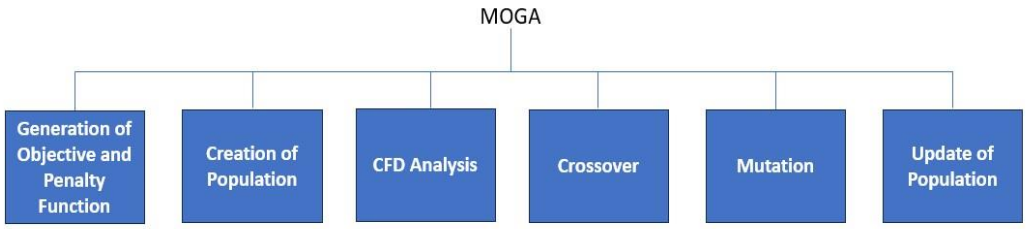

Figure 2.5. Transactions at MOGA [66]

Firstly, an objective function is created to determine the priorities of the output parameters to be optimized, and a penalty function is created if there are strict conditions. MOGA can then predict the values of the response variable for different values of the design variables, using the results of the response surface. These designs and results are used to create the initial population. This population contains a set of values of the design variables. Afterwards, MOGA selects the best performing spots, which are also called as “dominant zone”, because these points are passed to the next generations. Then, the selected points are crossed. Crossover is the process of shuffling the features and data of those points to create new design points.

MOGA then mutates the points slightly and creates new clusters to increase the probability of finding optimal design points, increase the diversity of the population, and help optimal design points to escape local minimums. Finally, mutated points are added to the population. Then, the best fitting points in the population are selected and the process is repeated until MOGA finds the desired optimal design points.

Moreover, MOGA is an evolutionary optimization technique which is generally used to solve multi-objective optimization problems [65]. Multi-objective optimization involves optimizing objectives that are more than single simultaneously, where improving one objective may lead to the degradation of another. In this thesis, the design objectives are listed below.

$$MOGA\begin{cases} Increase\ Pressure\ Recovery\ Ratio \\ Minimize\ Drag\ Coefficient\ of\ the\ Nacelle \end{cases}$$

Overall, MOGA optimization in Ansys Workbench provides me in this thesis to efficiently explore a wide range of design possibilities between selected design point parameters.

As mentioned before, creating an objective and penalty function is the first step of MOGA. According to Chong and Zak (2001), an objective function is a function that is to be minimized or maximized under a set of constraints. This function can also be considered as the output parameters that the optimization algorithm tries to improve [56]. It is a mathematical function that defines the quantity or value you want to maximize or minimize in each problem. It can be thought as the representative of the goal in solution and optimization process. As mentioned before, the first step of the optimization procedure is to define an objective function that determines priorities of objectives. In this thesis, maximizing pressure recovery ratio at fan area and minimizing the drag coefficient of the nacelle body constitute the objective function.

Moreover, a weighted sum approach is used to assign the weights of each objective which are based on their importance. In the weighted sum approach, set of goals in

objective function are scaled into a single goal by multiplying each objective by a user-supplied weight. This method is one of the common techniques in design optimization procedure. However, weight of each objective should not be selected randomly. Therefore, especially in multi-objective optimization problems, it should be well determined which desired output will be given more importance and which will be given less.

In my thesis, the weight for pressure recovery ratio is typed as w_1 and the weight for drag coefficient as w_2. Then, the combined objective function definition can be written as follows.

$$F_{objective} = w_1 \times Increasing\ Pressure\ Recovery\ + w_2 \times Reducing\ C_D \quad (2.40)$$

This term representing the weight of the first parameter which is the pressure recovery experienced by the fluid between the stream and fan section of the nacelle. The goal here is to maximize this ratio. Therefore, the objective section in Ansys Workbench, the option called “maximize” is selected.

As the aircraft moves through the air, drag force is experienced over the nacelle body as other sections of the aircraft. A lower drag coefficient is desired for lower fuel consumption as well. So, the goal is to minimize this coefficient. Therefore, the objective section in Ansys Workbench, the option called “minimize” is selected.

There are weighting factors which are w_1 and w_2 in the equation and those are assigned based on the priorities of the outputs. Within this manner, a higher value is given to the parameter having more priority. In this method, the sum of the weights should be equal to “1”.

By using this objective function, optimization algorithm is to find an optimum design compared to the baseline nacelle design while creating a balance between pressure recovery ratio and drag coefficient. The optimization algorithm looks for better design points that will provide the best balance and efficiency between these two goals. Moreover, the formulation and weighting of the objective function

might involve more complex considerations in case of any other objectives and constraints.

Since the higher priority is to increase the pressure recovery ratio and lower priority is to reduce drag coefficient in this thesis, a higher weight for the pressure recovery ratio (w_1) and a lower weight for the drag coefficient (w_2) are assigned. The exact values of w_1 and w_2 will depend on the specific emphasis. As forementioned before, this approach is to normalize the weights so that their sum is equal to 1. According to the importance, coefficients of w_1 and w_2 are assigned as follows.

w_1 = 0.75 (indicating higher priority for pressure recovery ratios)

w_2 = 0.25 (indicating lower priority for drag coefficient)

From above, it is stated that the importance of increasing the pressure recovery ratio value is 3 times more than the importance of decreasing the drag coefficient value. These w_1 and w_2 guide the optimization algorithm procedure, and the results obtained from calculations might vary depending on the chosen values of coefficients. Some adjustable changings could be made according to results after the initial selections on weights.

Moreover, optimization includes changing some design variables within CFD model. These variables can include geometric dimensions, boundary conditions, material properties, or any other factors that affect the fluid flow behaviors on body. In this thesis, inlet part is tried to be optimized in terms of given objectives.

In addition to the objective function, there could be some constraints that limit the range of allowable design variables. Constraints are important because they represent real-world limitations that must be considered during the optimization process. In this thesis, constraints include the variation range which is the lower and upper limits of the points forming the nacelle shape. This variation range is shown in further stages.

2.4 Design Objectives

The design objectives are the desired parameters that are implemented into the objective function which is a mathematical expression for the optimization algorithm. Since there are two-design objectives, the formulation is called as multi-objective optimization. Objective function is kind a definition of the physical explanation of the optimization process. As previously explained, the sum of the weights of the objectives must equal to "1". The coefficients of the parameters are given according to the importance of the desired outputs. Since the pressure recovery ratio has higher value in my thesis, it has a proportionally higher coefficient than the coefficient of the drag coefficient of nacelle body.

Objective function is given as below which is written as weighted sum approach.

$$\text{Objective(x)} = \sum_{\text{i=1}}^{\text{n}} \text{w}_\text{i} \left(\frac{\emptyset_\text{i} - \emptyset_\text{min}}{\emptyset_\text{max} - \emptyset_\text{min}} \right) \tag{2.41}$$

where w_i, n and $\emptyset$ represents the weights of parameters, number of objectives and values of the objective parameters, respectively. Since I have two design objectives, the objective function becomes,

$$\sum_{i=1}^{2} w_i = 1 \tag{2.42}$$

2.4.1 Pressure Recovery

The pressure recovery is the proportion of the total pressure of the fan section of the nacelle to the total pressure of the freestream. The pressure recovery has an important meaning in nacelle design since it affects the engine efficiency and total thrust generation. The formula of the pressure recovery is given below.

$$\eta = \frac{P_{total,fan}}{P_{total,\infty}} \tag{2.43}$$

As the pressure recovery increases, the loss in pressure between sections decreases which is desired ingredient. Total pressure includes static and dynamic pressure. For incompressible flows, where density is constant and Mach number is less than 0.3, Bernoulli equation satisfies the total pressure [67]. However, if density is variable, isentropic formulations are used to find the total pressure.

2.4.2 Drag Coefficient

The drag coefficient is a useful quantity that is used to measure the drag or resistance of an object in a fluid environment. It is a measure of how much the object opposes the flow of the fluid. This coefficient is one of the most important factors in fuel consumption of an aircraft. In other words, reducing this coefficient has an important meaning in terms of fuel economy. The formula of the drag coefficient is given below.

$$C_d = \frac{D}{\frac{1}{2}\rho V_\infty^2 A} \tag{2.44}$$

where D represents the total drag force, ρ means density of the fluid, V_∞ represents the freestream velocity and A symbolizes the wetted surface area of the nacelle.

CHAPTER 3

VALIDATION STUDY FOR FLOW SOLUTIONS

In this chapter, a validation study for three-dimensional flow solutions for the baseline geometry which was briefly defined in the previous chapter in section 2.2.3 is discussed. Specifically, both suitable level of mesh resolution and turbulence model are determined to be employed in the shape optimization study that will be presented later.

First, the baseline nacelle geometry is described in more detail. Following that, the details for the flow domain, meshing, and boundary conditions are provided. A grid convergence study is performed determining the suitable level of mesh resolution. As mentioned before, whole process of the required steady flow computations in this thesis are done by using the commercial solver ANSYS Fluent. A comparison of the results given by the potential turbulence models to be used in the more costly design optimization study is also carried out. Comparisons are made using the pressure recovery ratio results of the reference study. Comparisons are also carried out using the drag coefficient for the nacelle.

3.1 Geometry and Solution Domain

In this section, the geometric details of the baseline nacelle model where the validation study is carried out is described first. The coordinates and ratios given in the drawings are taken entirely from the validation study. Then, the required computational domain created to solve the flow field of the model is introduced.

The model geometry is the nacelle shape of a turbofan aircraft, called the baseline geometry, taken from Reference [52]. The geometry is axisymmetric. The data points taken from this reference are joined with a spline and a 2-dimensional shape

is obtained. These points also define the design parameters with use of Bezier splines. The coordinates of these points are given below in Table 3.1. The geometry drawing is shown in Figure 3.1.

Table 3.1. Global Coordinates of the Nacelle Profile

Points	***X-Direction***	***Radial Direction***
P1	*0.0078m*	*0.8008m*
P2	*0*	*0.7756m*
P3	*0.1459m*	*0.7369m*
P4	*0.3264m*	*0.7575m*
P5	*0.5018m*	*0.7744m*
P6	*0.6927m*	*0.7839m*
P7	*1.0000m*	*0.7861m*

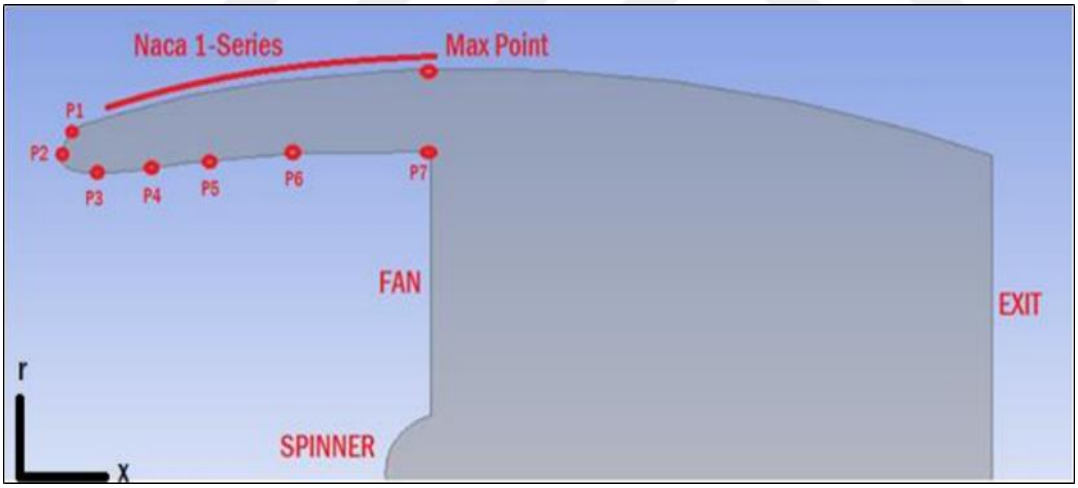

Figure 3.1. Nacelle Profile with Global Coordinates

In Figure 3.1, beyond point P1 over the outer surface, no explicitly given data was available and therefore a NACA-1 Series [68] profile is used to complete that part of the geometry. More specifically, NACA 16212 airfoil geometry is employed. The features of this airfoil are documented in NACA Technical Report 460 [69] [70].

The nondimensional coordinates of the NACA 16212 airfoil are given in Table 3.2.

Table 3.2. Some Data Points of NACA 1-Series

X/c-Coordinate	***10*Y/c-Coordinate***
0	0
0.12	0.24
0.18	0.36
0.24	0.48
0.36	0.72
0.54	1.08
0.72	1.44
0.84	1.56
1.0	2.0

These data points are fitted to the missing part of the outer surface of the nacelle. Then, the entire nacelle shape is parametrized by uniting it with cubic Bezier splines in the global coordinates defined in Figure 3.2. This is the beginning point for the advanced shape adaptations.

Right after generating the geometry according to Table 3.1, the proportional section of nacelle is drawn and shown in next page.

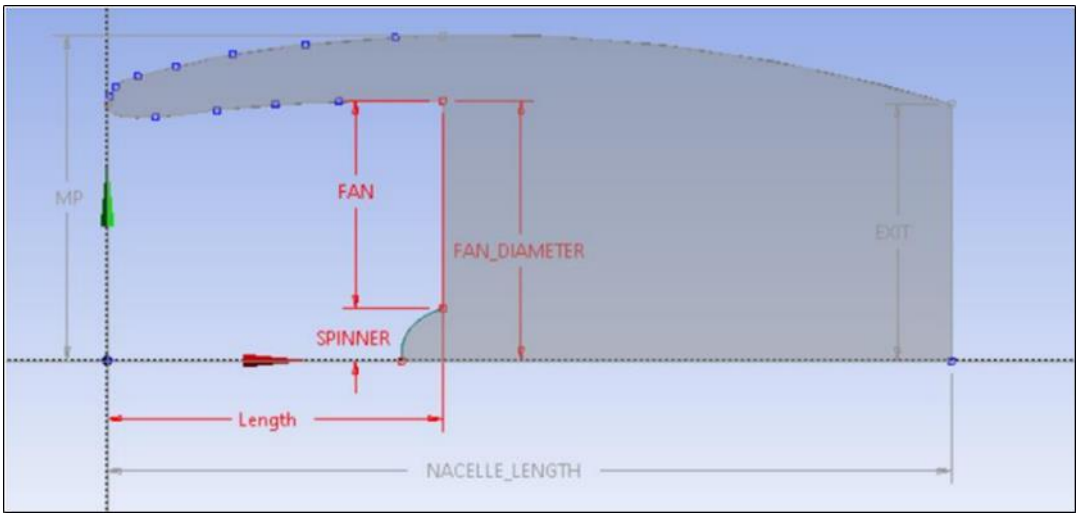

Figure 3.2. Global Dimensions of Nacelle Profile

Following the 2D shape creation, it is revolved in the azimuthal direction (around the x-axis) by 360° to form an axisymmetric 3D geometry, as shown in Figure 3.4.

More detailed information about the engine and nacelle type could be found in [52]. The proportions of the formed shape, which is schematically shown in Figure 3.3, are summarized in Table 3.3 given below.

Table 3.3. Global Ratios of the Different Sections of Nacelle

Section	***Ratio***
Length / Fan	*1.2722*
Nacelle Length / Fan	*3.2020*
MP / Fan	*1.2520*
Exit / Fan	*0.9873*
Spinner / Fan	*0.2000*

It should be stressed that all the geometric proportions used for the baseline geometry to be optimized are the same as those of the reference study [52].

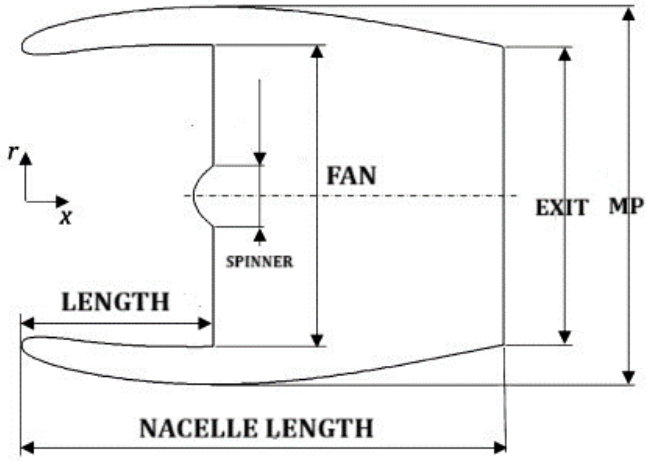

Figure 3.3. 2-Dimensional Axisymmetric Nacelle Profile [52]

Figure 3.3 also represents the schematic of two-dimensional profile of the nacelle body constructed using the design points and the NACA airfoil to complete the outer surface.

The revolved version of this geometry around the engine axis is the 3D model and shown in Figure 3.4.

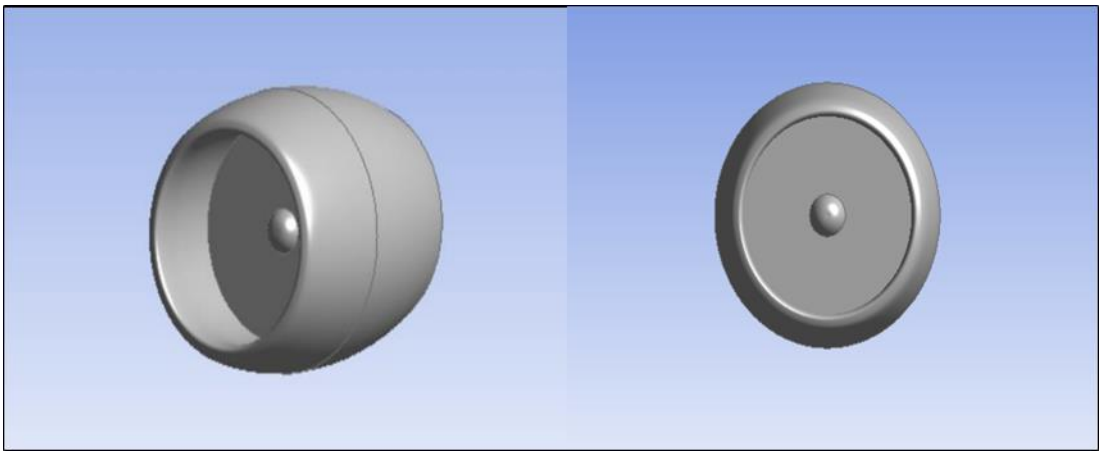

Figure 3.4. Three-Dimensional Nacelle Profile

The computational fluid dynamics (CFD) study is done over a limited volume containing the geometry, called the computational domain. This volume is discretized using nonoverlapping polyhedral elements [71] [72], called the

computational mesh, for the finite volume solution approach (FVM) available in the commercial Fluent solver.

When generating the computational mesh, there are some critical factors to consider. First, the grid resolution impacts the accuracy of the CFD simulation. Finer grids provide more accurate computations but also requires more computational time. Secondly, the distribution of the element sizes should be as smooth as possible to control the error levels. Several mesh quality check parameters are available in Fluent. As stated in the Ansys Fluent Meshing Guide, it is recommended that the orthogonal quality value for the structured mesh part over the geometry surface be not less than 0.1 for flow analysis [73].

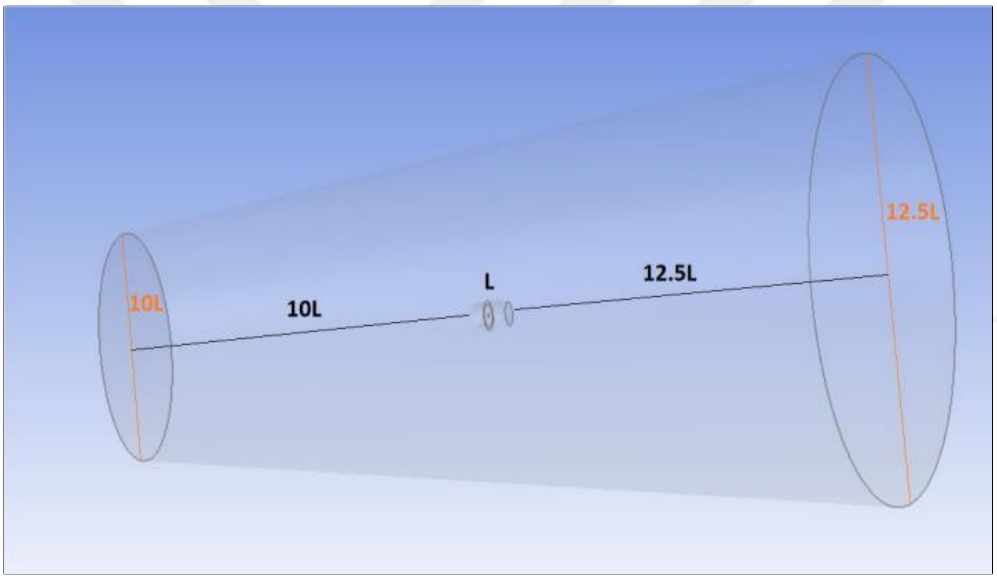

Figure 3.5. Control Volume of the Solver

The computational domain is sized in a conical shape as shown in Figure 3.5, with the upstream far boundary located at *10L*, and the downstream far boundary located at *12.5L* from the nacelle, where *L* represents its length. The diameter of the upstream far boundary is set to *10L*, while that downstream is set to *12.5L*.

3.2 Boundary Conditions

Boundary conditions have significant role in solving the computational problem such as assuring the accuracy and stability of problem. Their proper selection is needed for reliable results. The boundary conditions at the outer surfaces of the computation domain used for the air intake optimization problem at hand are shown in Figure 3.6.

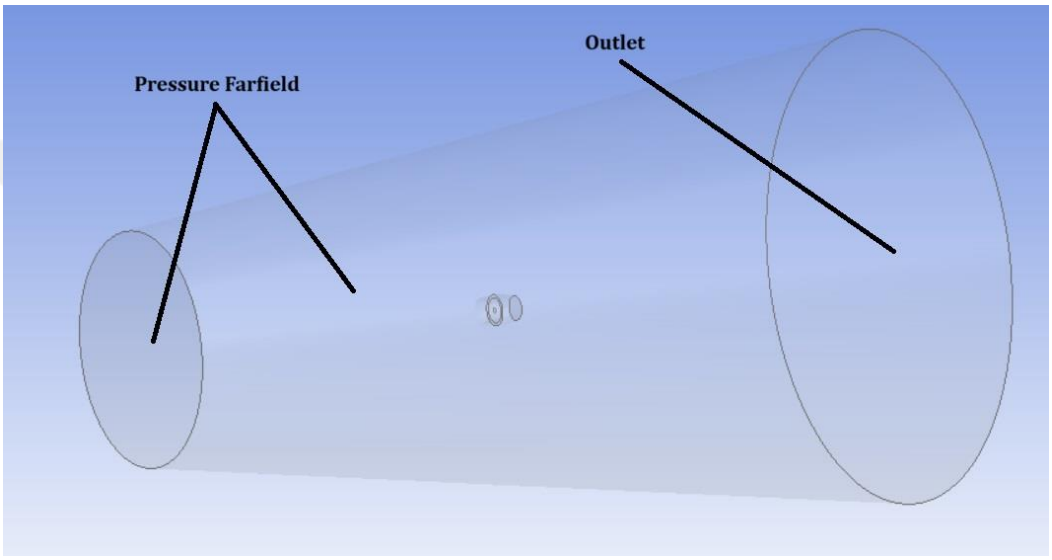

Figure 3.6. Boundaries of the Control Volume

In this figure given above, the outer surface surrounding the whole shape and the circled part in front represents the pressure farfield. The circle at the back represents the outlet.

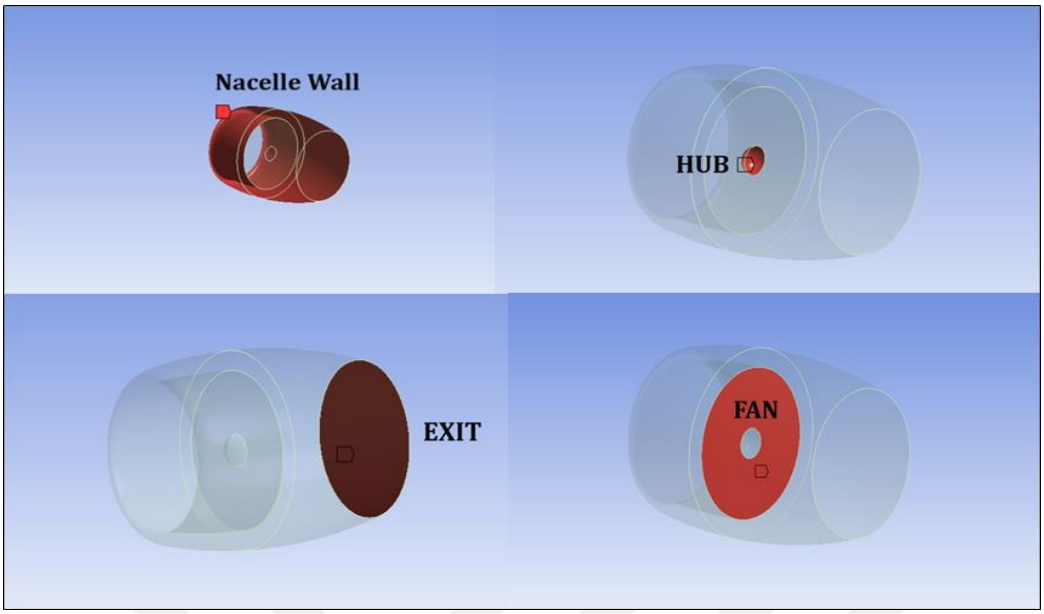

Figure 3.7. Boundaries of the Nacelle Profile

The other boundaries of the computational domain are shown in Figure 3.7. The boundary conditions imposed at the surfaces named as *HUB* and the *NACELLE WALL* in the figure are no-slip adiabatic wall condition. The air flow getting to the fan leaves the computational domain through the boundary named as *FAN* in the figure and therefore, outflow boundary conditions with specified mass flow rate are applied there. This flow gets back into the computational domain from the exit of the core and bypass of the engine named as *EXIT* in the figure. At this boundary inflow boundary conditions are used with specification of the same mass flow rate. The mass flow rate is given by,

$$\dot{m} = \rho V A \tag{3.1}$$

where ρ is density, A is the area of the fan blade surface and V is the mean axial velocity into the fan face boundary.

3.3 Flight Conditions and Solver Schemes

Since the flow validation is performed only at the climb condition right after takeoff, at which the Mach number is taken as 0.2, the density-based analysis is

chosen. Also, implicit formulation schemes are used with second order accuracy on turbulent viscosity to increase the accuracy. Molecular viscosity is computed using the Sutherland law which was given in Chapter 2. To accelerate the convergence of the solution, higher order term relaxation is used, as well. The used free stream parameters are given in Table 3.4, as referenced to [52].

Table 3.4. Flight Conditions for Climb [52]

Variable	*Climb*
Mach number *(M)*	0.2
Total Pressure *(P)*	101325 Pa
Temperature *(T)*	288.15 K
Angle of attack *(α)*	7°
Estimated mass flow rate *($\dot{m}$)*	1589 kg/s

3.4 Grid Generation

In a computational fluid dynamics problem, meshing is a discretization technique of the computational domain into smaller elements which are called as cells. The main task of the mesh is to solve the governing equations of fluid flow over the control volume. So, the more organized meshes there are, the more realistic the analysis results will be. However, having a high number of mesh does not always mean higher accuracy because this number should be controlled as it prolongs the solution time and computational costs as well.

Moreover, the quality of the mesh is critical to the accuracy for the accuracy of the results. Therefore, the orthonogal quality and the skewness parameters are checked in meshing processes which are responsible for the quality of the cells.

In this thesis, unstructured mesh type is selected for the flow computations, with triangular elements on the surfaces, prisms in the boundary layer, remainder of the volume is filled with tetrahedral elements. The generated grid has a total of 4

million elements, with a minimum orthogonal quality of 0.18, which is considered as acceptable. The reason why the number of meshes are chosen as 4 million will be explained in more detail in the mesh independence study section, which is one of the further stages.

The figures given in the next page represent the mesh structure on the nacelle surface in detail.

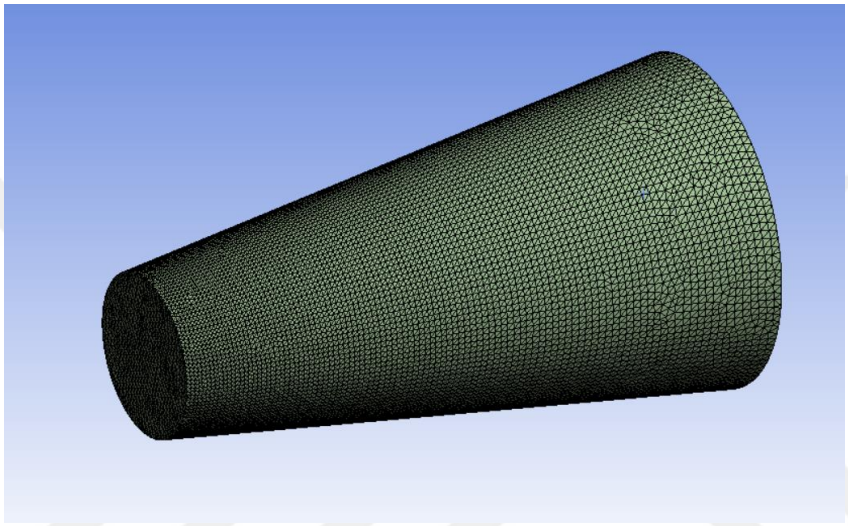

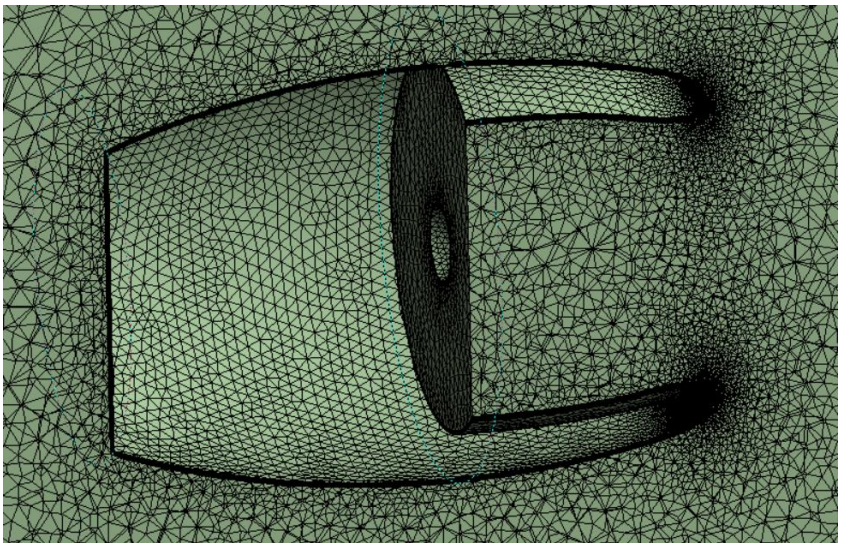

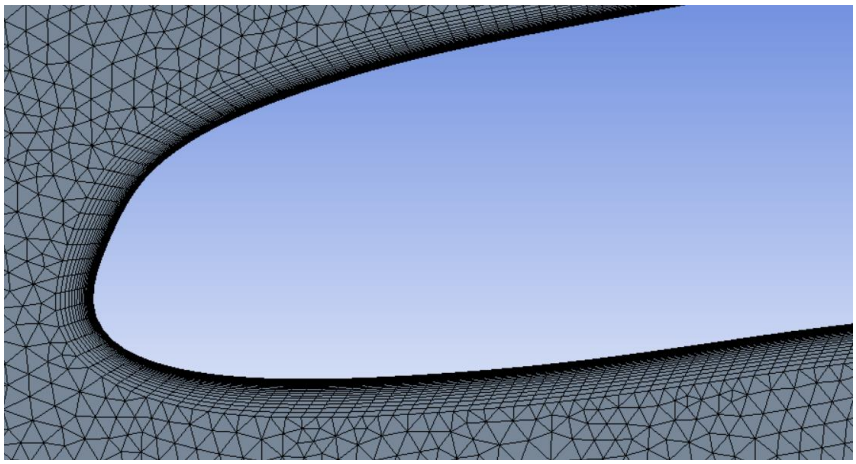

Figure 3.8. Mesh Structure

Also, the skewness value is less than 0.8 over the body and control volume which is another desired mesh quality to check. Since the viscous effects need to be calculated accurately, the boundary resolution is crucial. Within this manner, 40 layer of prism cells in the normal direction to the walls is grown in a controlled manner with ratio of 1.15 to handle it properly, with the maximum y^+ value less than 3.18, as will be demonstrated later as the outcome of the flow solutions. The meshing is shown from different perspectives in Figure 3.8.

3.5 Solver Parameters

In this section, the solver parameters used in analysis through this thesis are discussed. Pressure-based analysis type is not suitable for this model to observe the changes of the pressure value on the fan surface according to density throughout the analyses. Since the flow is compressible, density-based analysis type is selected throughout this thesis. Sutherland law is activated, which is described in previous sections, to understand the behavior of temperature on viscosity. Implicit formulation scheme is also selected. The value of 10^{-5} is chosen as convergence criteria for mass, momentum, energy, and turbulence solutions.

3.6 Mesh Independence Study

In this section, numerical studies are carried out at the climb condition specified in the preceding section to find the sufficient mesh resolution as well as to determine a proper turbulence model to be employed later in the optimization work.

A grid convergence study is a parametric study to assess the sensitivity and sufficiency of a computational fluid dynamics (CFD) simulation in terms of mesh resolution. The main aim of the mesh independence study is to determine the minimum mesh resolution required to obtain reliable and accurate results.

A mesh sequence of three different levels of resolution, named as *coarse* (1~2 million cells), *medium* (3~4 million cells), and *fine* (5~6~7 million cells) meshes are generated all with the same y^+ value of 3.18. The Spalart-Almaras turbulence model is chosen for the study. The computed total pressure recovery ratio results are compared in Figure 3.8. The results indicate that the pressure recovery does not change significantly after 6 million meshes. However, since the computational time also increases with the number of elements, 4 million element is selected for further calculations.

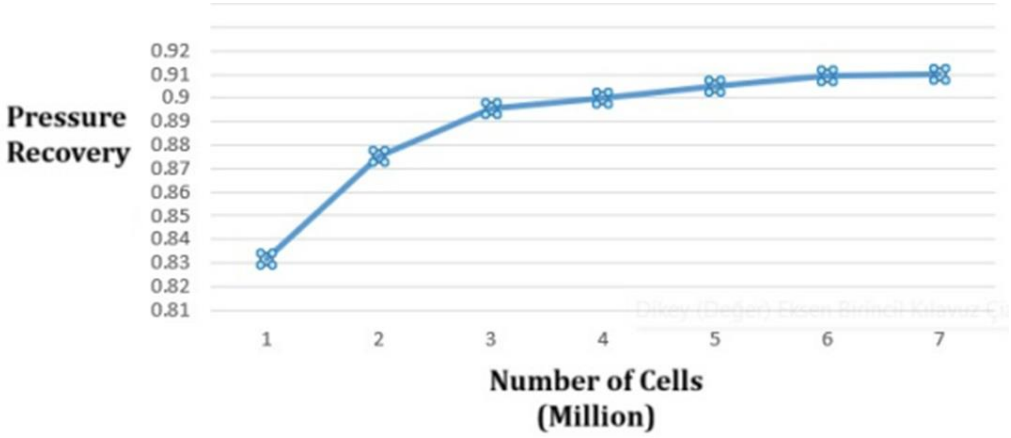

Figure 3.9. Grid Convergence Results

Following determination of a proper grid resolution for the flow solutions, more detailed comparisons of the attained results are carried out to available literature data in this section. Since in the optimization work the objective function is constructed as weighted sum of the total pressure recovery ratio and drag penalty, special care here is placed in comparison of these two outcomes of the computed flow fields. Although it is not one of the objectives, the maximum Mach number on the nacelle inlet is also compared to check the accuracy of the analysis results.

The total pressure recovery ratio contours of the reference work [52] and the present calculated ones are shown in Figure 3.10, and 3.11, respectively. While the minimum pressure recovery value is 0.68 for the literature data, it is found to be 0.702 in the present study.

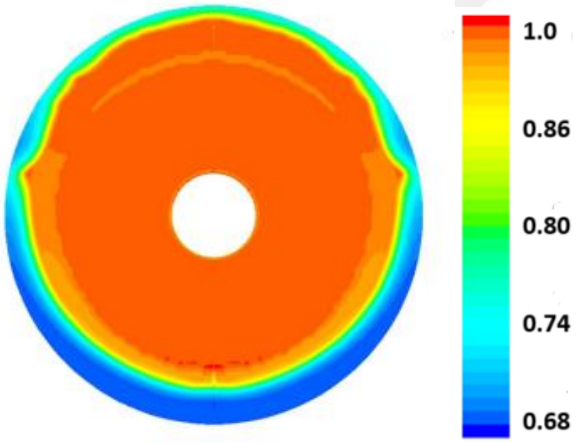

Figure 3.10. Pressure Recovery Results on Reference Paper [52]

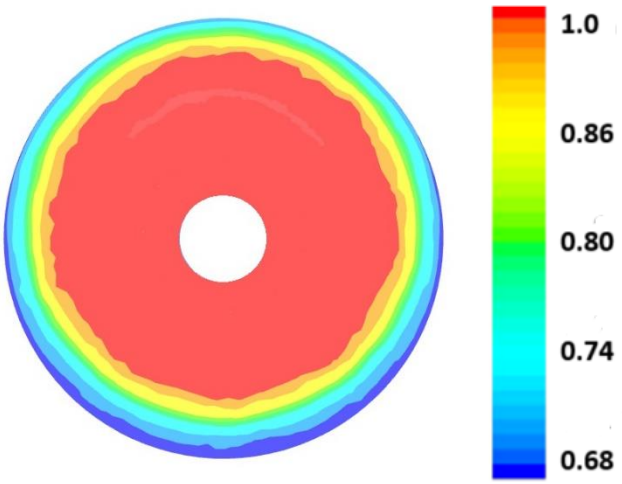

Figure 3.11. Pressure Recovery Results on Spalart-Allmaras Turbulence Model

The Mach number distributions in the meriodinal cut of the air inlet are shown in Figure 3.12. While the value of the maximum Mach number in nacelle inlet in the literature study appears as 1.65, it is computed as 1.57 in this study.

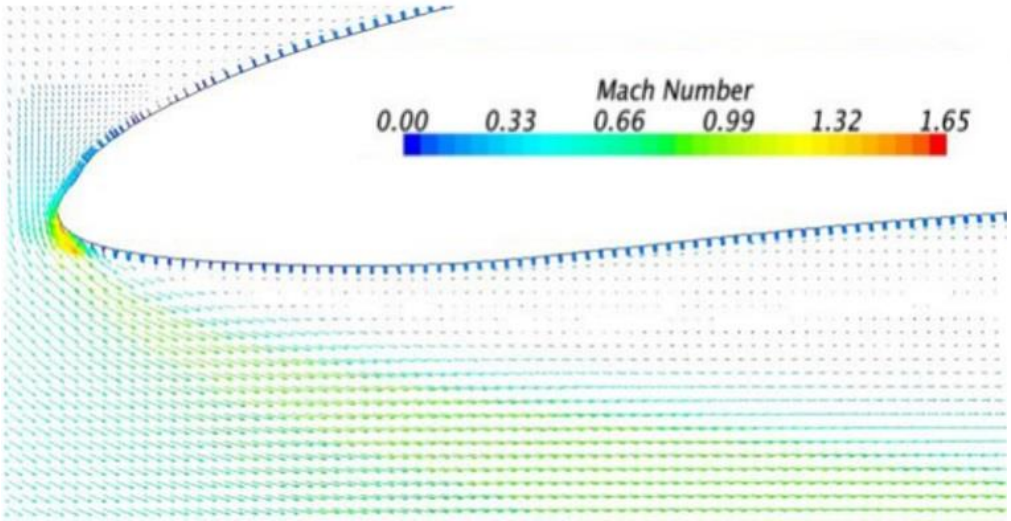

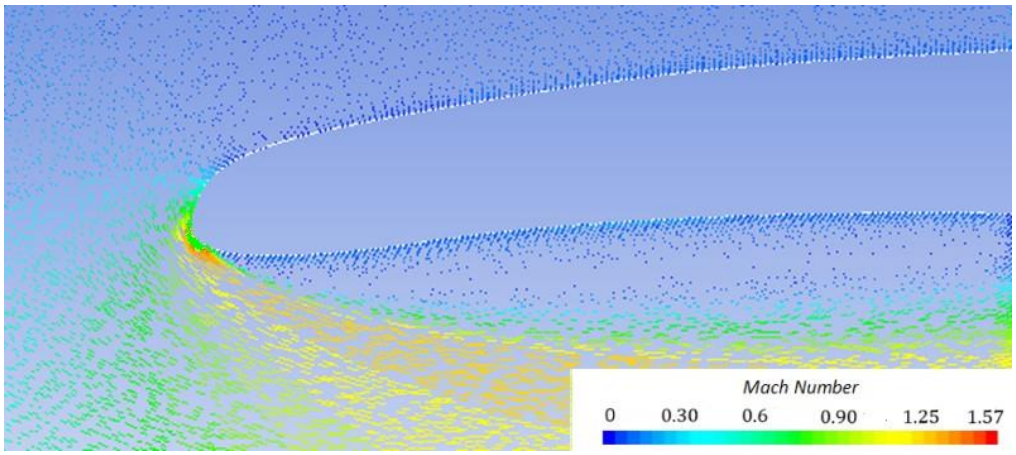

Figure 3.12. Mach Number Comparison of Reference Paper [52] and Baseline Model

In computational fluid dynamic problems, there is a dimensionless parameter that represents the distance from the first grid cell to the wall surface which is called as y^+[76]. It is used for determining the accuracy of the turbulence models near walls. When determining this value, the value assigned to the distance of the first cell right after the wall which is the distance from the wall is important and these calculations are done according to the formulas given below.

$$y^+ = \frac{yu_\tau}{\nu} \tag{3.2}$$

where y is the first cell distance from the wall, u_τ is the friction velocity and ν is kinematic viscosity of the fluid. Since the value to be assigned is y^+, the first cell calculation is made by revising the formula as,

$$y = \frac{y^+\nu}{u_\tau} \tag{3.3}$$

$$u_\tau = \sqrt{\frac{\tau_w}{\rho}} \tag{3.4}$$

where τ_w and ρ represents wall shear stress and density, respectively. Also, the calculation of the wall shear stress is done by,

$$\tau_w = \frac{1}{2}\rho U_\infty^2 C_f \tag{3.5}$$

where U_∞ and C_f represent the free-stream velocity and friction coefficient.

The y^+ value ranges from 1 to 30, which is generally considered appropriate for most turbulence models [75] [76]. Too high or too low y^+ values may cause solver to estimate the properties at boundary layer inaccurately.

The figures shown below shows the y^+ values over baseline the nacelle body.

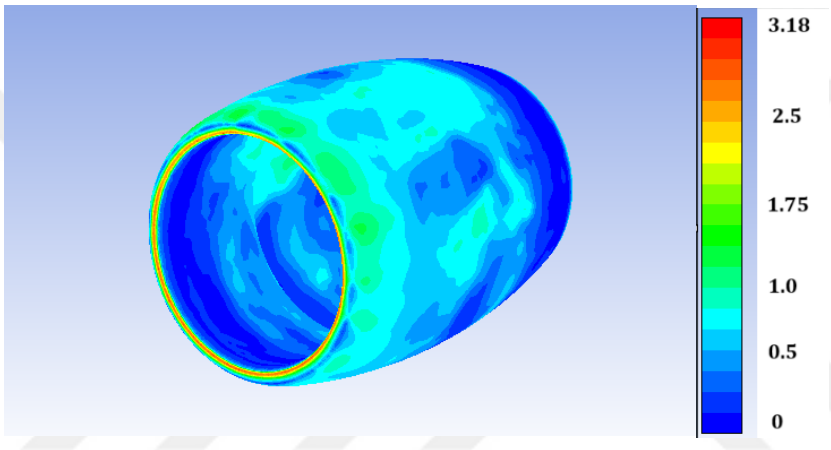

Figure 3.13. y^+ Values on Baseline Nacelle Body

3.7 Turbulence Model Selection Study

In this section, the effect of the chosen turbulence model on the results are evaluated. The Spalart-Allmaras, Realizable k-ϵ with enhanced wall treatment and SST k-ω models are used to investigate the pressure recovery ratio results. The required computational time is also assessed in terms of the potential cost of the turbulence model to the wider optimization study to be carried out. Since there is no available data for drag coefficient on the computed geometry, only the pressure recovery ratio is used for the evaluation. Interpretation of the drag coefficient results is made in further stages. For flow convergence, the pressure, momentum, energy, and turbulence equations are iterated until the normalized residual is reduced to 10^{-5}. Convergence on the mesh with about 4 million elements which

was determined following the grid convergence study at the climb condition is usually achieved after approximately 4300 iterations. A total of 12 CPUs were used for the calculations. The computed pressure recovery ratio values and the computational times are shown in Table 3.5.

Table 3.5. Differences of Turbulent Flow Solvers on Climb Condition

	Spalart-Allmaras	*Realizable k-ϵ*	*SST k-ω*	*Experimental Data*
Pressure Recovery Ratio	0.9081	0.9124	0.9133	0.921
Computational Time	11 hours	14.5 hours	16 hours	-

When the results in the table are compared with those of the reference, it is observed that the most accurate result is provided by the SST k-ω model. In this respect, this is the actual turbulence model that one normally should choose for the computations. However, the optimization algorithm requires many analyses, and the difference in the total pressure recovery ratio is not excessive but the computational time is the least for the Spalart-Allmaras turbulence model. Therefore, the Spalart-Allmaras turbulence model is the one chosen for the rest of the work in the thesis.

3.8 Effects of Angle of Attack

Following the verification study on the baseline geometry presented in the preceding section for an identical case found in literture, the values of the angle of attack and temperature are changed here in this section. Both cruise and climb situations are studied. The cruise condition, pressure and temperature values are based on an altitude of 10 km. The conditions are given in Table 3.6. At climb an angle of attack value of 8 degrees (7 degrees in literature), and at cruise a value of

2 degrees is considered. However, the mass flow rates are based on that from the reference study. The computations are done using the Spalart-Allmaras turbulence model.

Table 3.6. Different Boundary Conditions for Climb and Cruise Stages

Variable	*Climb*	*Cruise*
Mach number *(Ma)*	0.2	0.7
Total Pressure *(P)*	101325 Pa	26500 Pa
Temperature *(T)*	300 K	223.25
Angle of attack *(α)*	8°	2°
Estimated mass flow rate	1589 kg/s	643 kg/s

First, the analysis results on the baseline nacelle model in the climb stage are given.

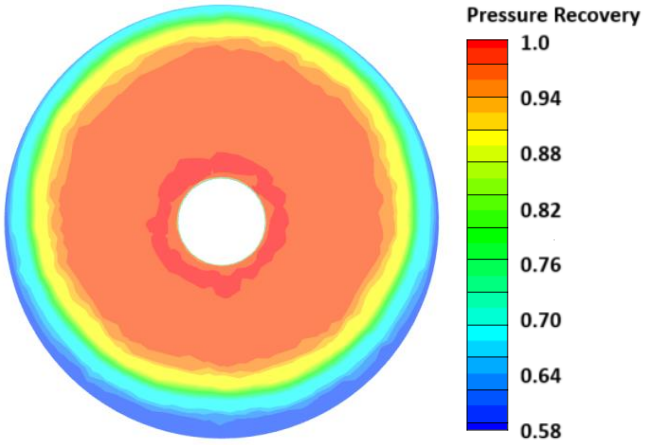

Figure 3.14. Pressure Recovery Ratios for Climb

Figure 3.14 shows the pressure recovery ratios over the fan surface of the baseline nacelle shape where the average value is found as 0.8702. It is clearly observed that 1 degree increase in the angle of attack value value from 7 to 8 degrees, reduces the pressure recovery value. This occurs because the minimum pressure area represented by the dark blue region at the bottom of the fan surface is increased.

The asymmetry is due to the angle of incidence. The effects of the boundary layers on the pressure distribution are clearly seen.

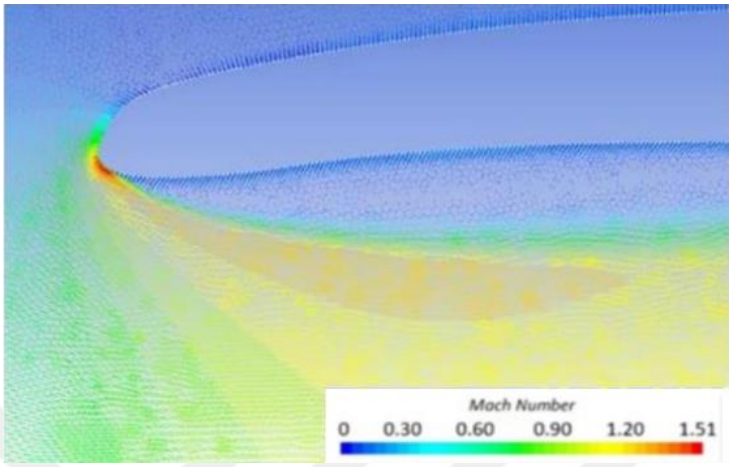

Figure 3.15. Vector Scales over the Nacelle Inlet for Climb

In Figure 3.15, the Mach number distribution in the vertical meriodinal cut is shown. In the lip area in a narrow volume flow gets supersonic.

Now, the results for the baseline model at the cruise condition are given. Figure 3.16 gives the total pressure recovery ratio values. As expected, since the angle of attack value is lower during the cruise, the boundary layer is thinner and the values are more uniform at the fan. The aim here is to provide even smoother distribution by the optimization work.

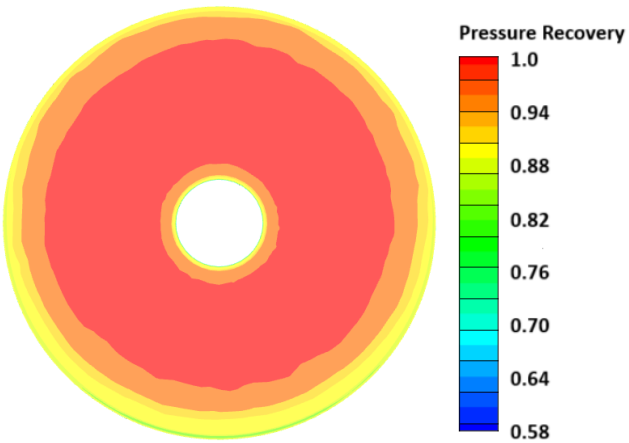

Figure 3.16. Pressure Recovery Ratio Results for Cruise

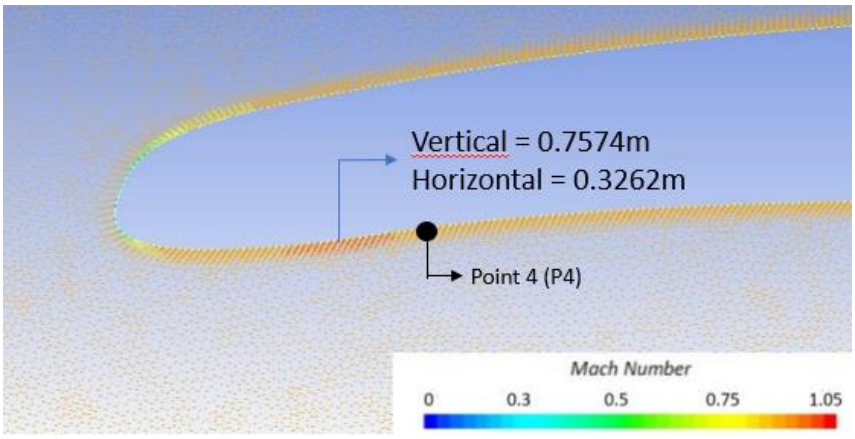

Figure 3.17. Vector Scales over the Nacelle Inlet for Cruise

In Figure 3.17, the point where the maximum Mach number occurs is shown with its coordinates, and this point is close to the P4. In the following stages, it is examined how the location of this point changes after optimization.

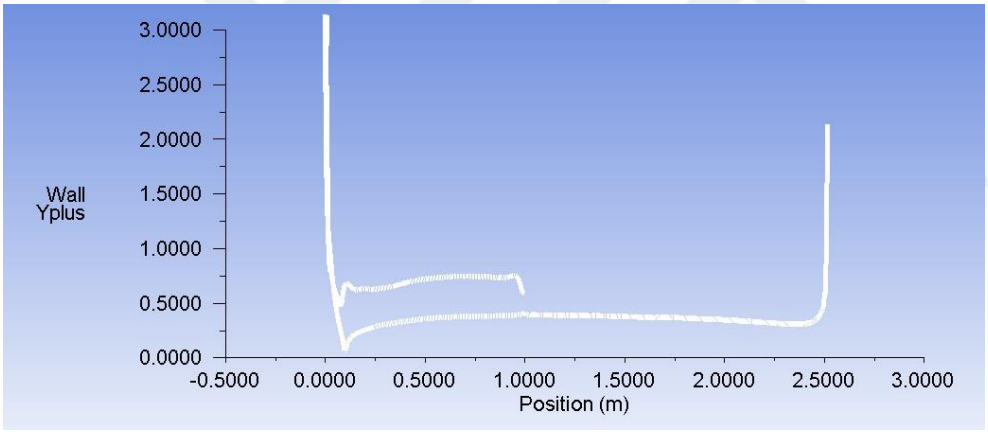

Figure 3.18. y^+ Values Over Nacelle Body by Position

Figure 3.18 shows how the the y^+ is distributed with the axial position at the nacelle wall. The maximum value is found as 3.18 which is acceptable. In most part over the nacelle wall y^+ values seem closer to 1.

Moreover, the drag coefficient of the nacelle body which is the second output parameter is investigated. However, there is no information in the literature as no drag coefficient study has been carried out in the reference nacelle design. In this manner, publications in the literature that calculate the nacelle drag coefficient for

turbofan engines which are similar to the reference shape are examined to get an idea in climb and cruise conditions.

In drag coefficient calculations of the nacelle body, the frontal area of the nacelle is generally used which is defined as the projected engine area in the axial direction. Wetted area is the total surface area of the nacelle in contact with the fluid. This area can also be used to calculate the nacelle drag coefficient.

Table 3.7 shows the nacelle drag coefficients for different types of turbofan engine at climb and cruise stages at various conditions, for climb at Mach numbers of 0.2-0.3 and angles of attsck of 5-8°, and for cruise at Mach numbers of 0.7-0.8 and angles of attack of 1-3°. It should be noted that the frontal area was used for the drag coefficients presented in the table.

Table 3.7. Drag Coefficient Values of Similar Shapes Found in Literature (based on frontal area) [58] [59] [77] [78] [79]

Aircraft Type	*Nacelle Type*	*Drag Coefficient (Climb)*	*Drag Coefficient (Cruise)*
Airbus A320	Classical	0.05	0.04
Airbus A330	Classical	0.05	0.04
Airbus A350	Vortex Generator	0.04	0.03
Boeing 737	Classical	0.05	0.04
Boeing 747	Classical	0.06	0.05
Boeing 787	Vortex Generator	0.04	0.03

The drag coefficient numbers given in the table above have been compiled from various sources found in literature [58] [59] [77] [78] [79]. These numbers are values obtained under ideal conditions. In real conditions, the drag of the nacelle may vary depending on factors such as environmental factors and details of the nacelle design. Actually, it is not possible to compare the reference design by completely adhering to these values, but it helps us to get a preliminary idea for the analyzes.

Table 3.8 shows the computed drag coefficients for the studies baseline geometry at the climb and cruise conditions based on the engine frontal area. The values are similar to those given in Table 3.7 compiled from literature.

Table 3.8. Computed Drag Coefficient Values for the Present Baseline Nacelle (based on frontal area)

	$C_d\ (Climb)$	$C_d\ (Cruise)$
Reference Nacelle Shape	0.0481	0.0387

CHAPTER 4

OPTIMIZATION RESULTS AND DISCUSSION

In this chapter, the design optimization study by Multi-Objective Genetic Algorithm (MOGA) is discussed with presentation of the attained results. In the study first model creation is performed by Bezier spline connections of the design control points. Then, the model is subjected to flow analysis using the commercial flow solver program ANSYS Fluent to obtain the pressure recovery ratio over the fan surface and drag coefficient of the nacelle body that form the objective function for the optimization work. This is done repetitively for a defined set of control points that are distorted from those of the baseline shape. The purpose of doing this is to examine the effects of the change to each design point on output results, that is to create a response surface. This forms the first population set for the MOGA algorithm. Then, MOGA creates new clusters and populations by crossing the design points in this population among themselves and tries to produce more optimal points according to the desired output results, and the process is repeated in this way until the most optimal design is achieved.

Table 4.1 shows the lower and upper bounds for the design points selected for creation of the response surface. To avoid the line continuity problem, it is necessary to ensure that the curvature and slope values of the splines change gradually in the nacelle entrance region. The recommended curvature and slope values are 0.1 to 0.5 and 0.01 to 0.05, respectively [6]. The values in the table above are created to stay within the specified ranges and avoid line continuity problems.

Table 4.1. Ranges of Input Variables for Optimization

Parameters	Lower Bound	Baseline Selection	Upper Bound
P2V	0.76	0.7756	0.78
P3H	0.12	0.1459	0.18
P3V	0.73	0.7369	0.76
P4H	0.30	0.3264	0.35
P4V	0.75	0.7575	0.79
P5H	0.48	0.5018	0.52
P5V	0.76	0.7744	0.78

Then, the relationship between the parametric inputs located on the designed shape is checked to create a correlation for the output parameters. The correlation values are shown In Figure 4.1. When a value in the color bar approaches positive 1 a strong positive correlation is observed between the points, while approaching to negative 1 a negative correlation exists.

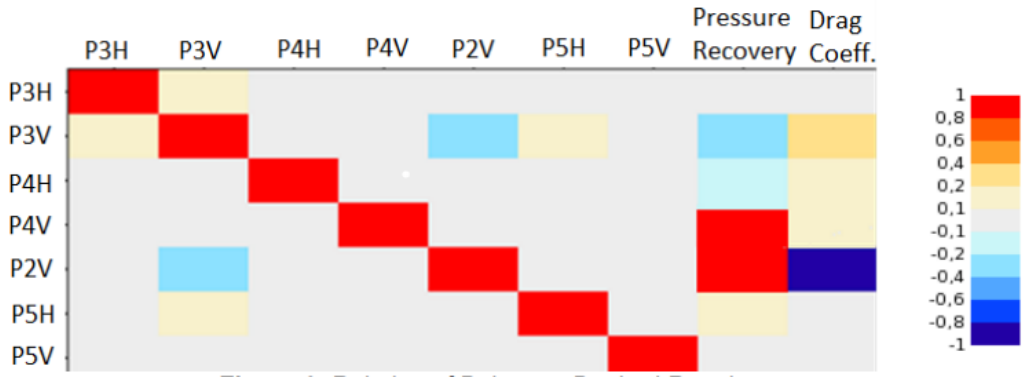

Figure 4.1. Relation of Design Points on Output Parameters

It is observed from these results that the most effective way to increase pressure recovery ratio is to make changes on P2V and P4V points which represents the vertical changes on P2 and P4 control points. These points are in the front and middle parts of the nacelle inlet. Also, changing points P5H and P5V can also increase pressure recovery, but not as effective as variations of P2V and P4V. The

most crucial point seems here as P2V, which represents vertical deflections for P2, because changes to be made at this point may significantly increase the pressure recovery ratio but may also lead to an undesirable result such as an increase in the drag coefficient value. Therefore, changes to be made at this point should be carefully examined according to the analysis results.

These correlation of parameters between each other is used for prediction success of optimization process because process learn the dynamics of shape and its solution with training data samples. In this manner, 80 different sample points which are between the specified lower and upper bounds shown in Table 4.1 are solved at the same conditions with the same solver parameters. A data projection is generated inside the tool of Ansys.

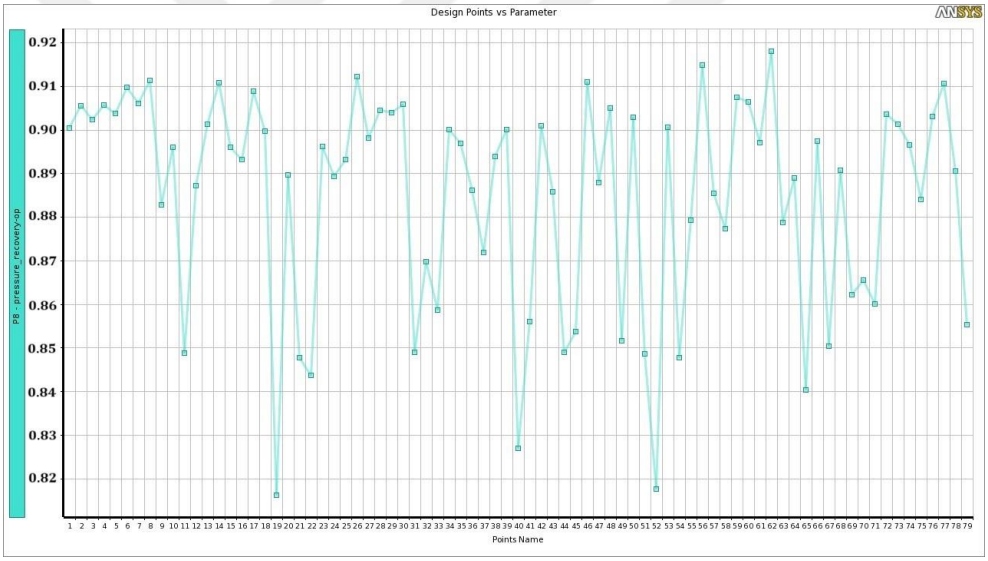

Figure 4.2. Different Control Point Results on Pressure Recovery

The predicted values of the pressure recovery related to the 80 different control points are shown for the climb condition in Figure 4.2. These points were obtained by variations of 7 parametric points on the previously mentioned nacelle shape, and the same analysis was repeated for 80 different samples.

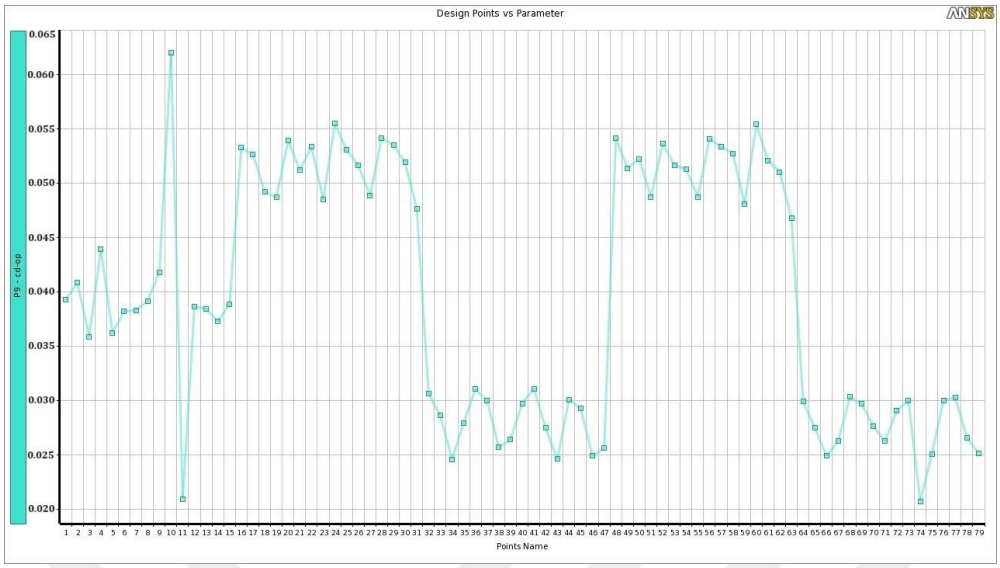

Figure 4.3. Different Control Point Results on Drag Coefficient

Similarly, the same procedure is done for drag coefficient calculations and shown in Figure 4.3.

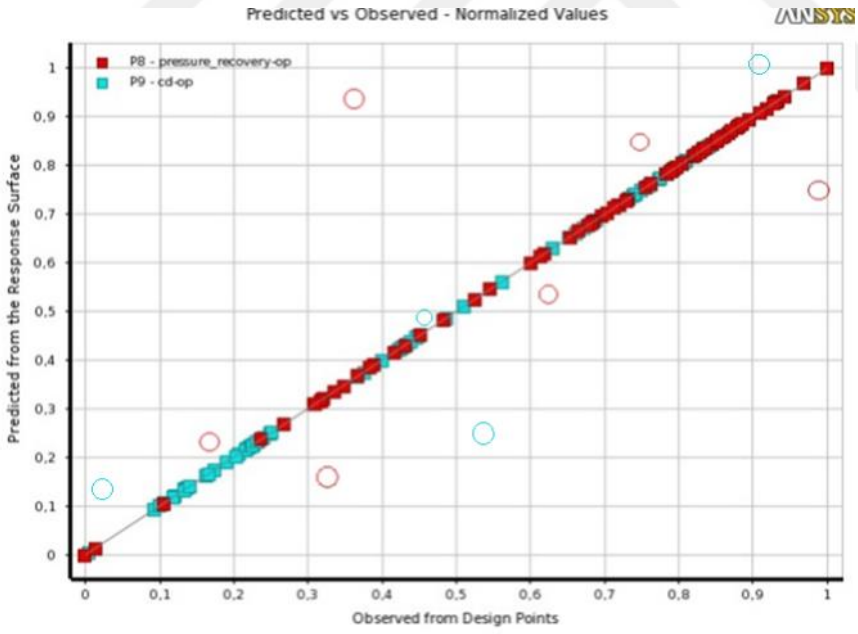

Figure 4.4. Cross-Validation Application for Initial Samples

Then, the cross-validation application is done for initial samples for optimization procedure because this technique helps to make the optimization process more

efficient. The results of this procedure are shown in Figure 4.4. The correlation rate is calculated as 0.9243 which is quite acceptable. In this technique, all the data is divided into clusters of equal size. Then, clusters are used as the training set and the remaining clusters are used for testing. The optimization algorithm is trained and evaluated on the test set. This process is repeated simultaneously, and a different set is used as the test set in each iteration. In the process of shape optimization with parameter variation, this technique can be used to find the best values of the parameters. This can make the algorithm work more efficiently.

Following this, a sensitivity analysis is done for various purposes such as identifying the most important parameters over the nacelle shape. This helps make the optimization process more efficient. Also, the sensitivity analysis is done to understand how the parameters affect the performance of the design such as the efficiency of output parameters such as response surface. Also, this shows how each parameter affects the performance of the design. The graph given in Figure 4.5 shows how a small change in the value of the parameter affects the change in the performance of the design. This helps in taking measures to improve the performance of the design. Also, Figure 4.5 shows the sensitivity of design control points on output parameters for climb condition.

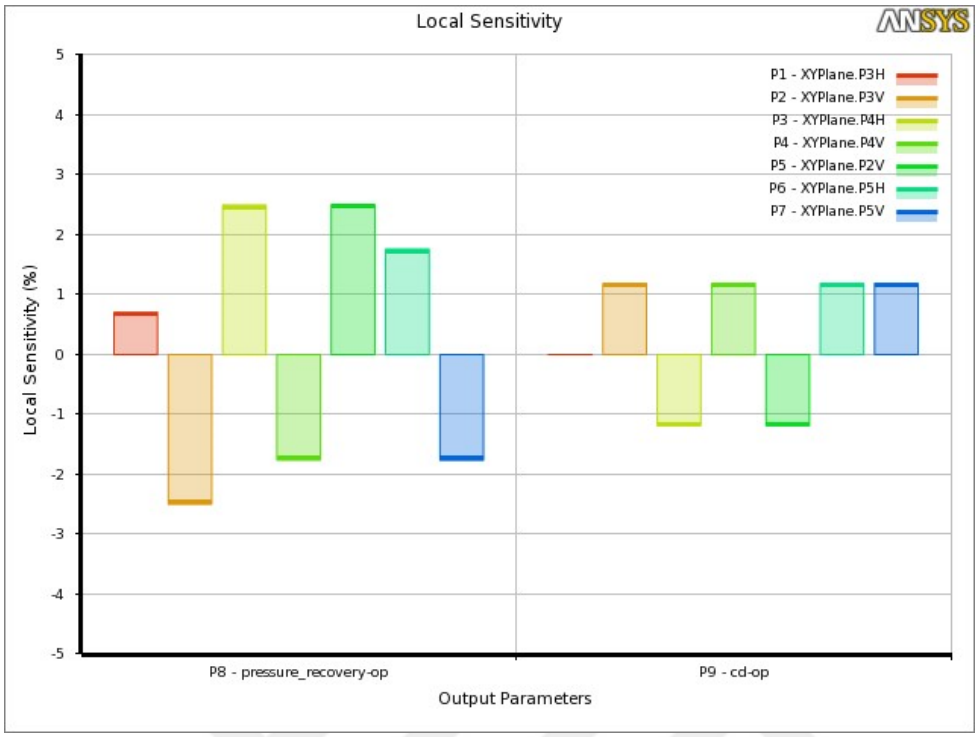

Figure 4.5. Local Sensitivity of Design Control Points on Outputs for Climb

As the value of P3V parameter increases, the nacelle shape becomes more inclined, reducing pressure recovery. Similarly, as the value of P5H parameter increases, the nacelle shape captures more air, which increases pressure recovery ratio. However, the changings of this point may disrupt the behavior of the air near nacelle body which may result in drag increment which is not a desired outcome. Moreover, some of the points affect the sensitivities in a negative way for both output parameters. For example, the changings in P5V drops the pressure recovery and increases the drag coefficient of the nacelle body which are both undesired outcomes. Similarly, every point on the chart can be interpreted on the effects on output parameters. Therefore, this interpretation should be done correctly.

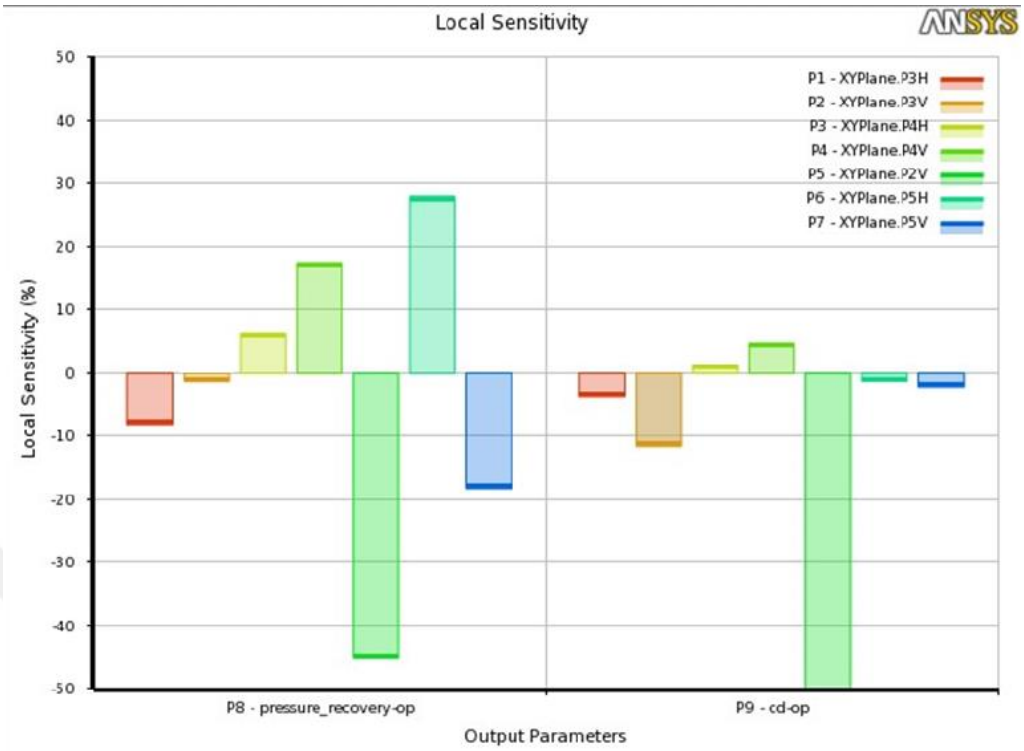

Figure 4.6. Local Sensitivity of Design Control Points on Outputs for Cruise

The local sensitivity of each design point is shown in Figure 4.6 for the cruise analysis. As it can be seen, the effect of the vertical changes in P5 results in loss of pressure recovery for both cases. Therefore, the current design point can be considered the most optimum value for design. However, since not only a single point but multiple points are optimized here, combinations of changes to those 7 control points shown in Table 4.1 can create a positive result. Also, the P2V which is responsible from the curvature of the frontmost point has enormous meaning and the selection of this point should be selected specifically for the desired output values since the variations of this point affect the pressure recovery and drag coefficient in a both negative and positive way, respectively.

Following all these, the Multi-Objective Genetic Algorithm (MOGA) is started to find the optimal locations for each point. This optimization technique is designed to optimize multiple parameters that affect the performance of a design such steps as population generation, selection from population, crossover, mutation and updating

the population which are all discussed in previous chapters. These steps are repeated until the most optimal shape having desired outputs are found. As mentioned before, MOGA algorithm in Ansys utilizes from response surface to estimate the relationships between parameters that affect the performance of the design. This allows MOGA to search for optimal spots more efficiently.

Within this manner, the results of MOGA optimization from the combination of RSM with Kriging method is listed below for both climb and cruise conditions. Briefly, Kriging method is a statistical approach that estimates the relationships between parameters that affect the performance of a design. This approach works on a set of points that represent the values of the design parameters. First, MOGA fills the research space with random populations including different design points. Then, Kriging predicts potentially well-performing regions of the research space based on CFD calculation results at these points. After that, MOGA examines these regions in more detail by performing further CFD calculations until optimization algorithm meets requirements.

The optimization algorithm has converged after 8962 and 13609 iterations for climb and cruise, respectively.

Moreover, the Pareto and stability percentages of the MOGA optimization is checked for both cases as well to observe the reliability and decisiveness of the design where the percentages are 12% and 17.98% respectively for climb condition. Pareto percentage indicates that optimized nacelle design provides a 12% improvement over the standard nacelle design in terms of objective function weightings and output parameters. This may seem like a small improvement, but the significance of this improvement is shown with tabulated data in next page. Moreover, stability percentage show the stability of the optimized design where the optimized nacelle is nearly more stable than baseline model by nearly 18%. Within the same manner, the Pareto and stability percentages of the optimized nacelle is found as 17% and 4.7% respectively for the cruise stage which indicates that indicates that MOGA has found a more optimal shape.

In Table 4.2 and Table 4.3, candidate points for more efficient output results are written. While creating these tables, the coordinates of the 3 candidate points given by MOGA, and the estimated values of the output results are given. The thing that needs to be emphasized in this part is that these candidate points and their output results need to be verified, because these are only the estimated values of the optimization algorithm, and it is necessary to verify and check the accuracy of the algorithm. If the values obtained right after the verification analysis are close to the estimated values, it can be said that the algorithm works properly.

In this regard, *Candidate Point 1* is implemented into the analysis to compare the accuracy of predictions by MOGA. Moreover, the accuracy of the optimization algorithm is established for both climb and cruise conditions. While performing this validation analyzes, only *Candidate Point 1* is employed, as mentioned before. These results are shared in the further pages.

Table 4.2. Candidate Points for Climb Condition

	Candidate Point 1	**Candidate Point 2**	**Candidate Point 3**	**Baseline Model**
P2V	0.7794	0.7754	0.7646	0.7756
P3H	0.1631	0.1722	0.1457	0.1459
P3V	0.7534	0.7314	0.7463	0.7369
P4H	0.3404	0.3044	0.3171	0.3264
P4V	0.7662	0.7653	0.7614	0.7575
P5H	0.4960	0.4814	0.5152	0.5018
P5V	0.7789	0.7719	0.7741	0.7744
Pressure Recovery	**0.9061**	**0.8968**	**0.9012**	**0.8702**
Drag Coefficient	**0.0432**	**0.0425**	**0.0414**	**0.0481**

Table 4.2 and 4.3 represent the candidate points that should be selected for the optimal models according to desired output parameters for climb and cruise, respectively.

Table 4.3. Candidate Points for Cruise Condition

	Candidate Point 1	**Candidate Point 2**	**Candidate Point 3**	**Baseline Model**
P2V	0.7741	0.7718	0.7794	0.7756
P3H	0.1219	0.1238	0.1237	0.1459
P3V	0.7601	0.7600	0.7600	0.7369
P4H	0.3013	0.3008	0.3016	0.3264
P4V	0.7786	0.7770	0.7666	0.7575
P5H	0.5137	0.5041	0.4988	0.5018
P5V	0.7794	0.7801	0.7790	0.7744
Pressure Recovery	**0.9712**	**0.9686**	**0.9602**	**0.9408**
Drag Coefficient	**0.0328**	**0.0297**	**0.0218**	**0.0387**

While creating these points, new samples are created as combination of initial samples, crossover, and mutation. Analyzes of 80 different points are performed on the response surface section, which enabled the formation of the optimization algorithm, and these points were used as initial samples. Then, number of samples per iteration is selected as 200 with maximum of 1000 iterations. All in all, number of evaluations for climb and cruise are seen as 13903 and 10387, respectively.

From the tables given above, it is clearly observed that the coordinates of the design points that provide the same mass flow rate for both climb and cruise conditions and make the output value more optimal are not same, and some points are even completely different. For example, it is observed that the P3V point should be higher from the coordinate system in the cruise condition and should even remain constant at a value of 0.76, while the same point can be located at different points with lower values in climb stage. Moreover, P3H point shows different behavior for climb and cruise stages as well. While the value of P3H variates between midsections of 0.14 and 0.17 in climb, this point should be close to 0.12 values for cruise stage.

Moreover, there is a visual representation (Figure 4.7, and 4.8) of the performance trade-offs between different design objectives which is called as trade-off chart in MOGA algorithm. It helps to understand the relationships between the objectives and make decisions about the design. Generally, points are colored or sized differently in trade-off charts to represent useful information, such as feasible design space demonstrating the achievable designs.

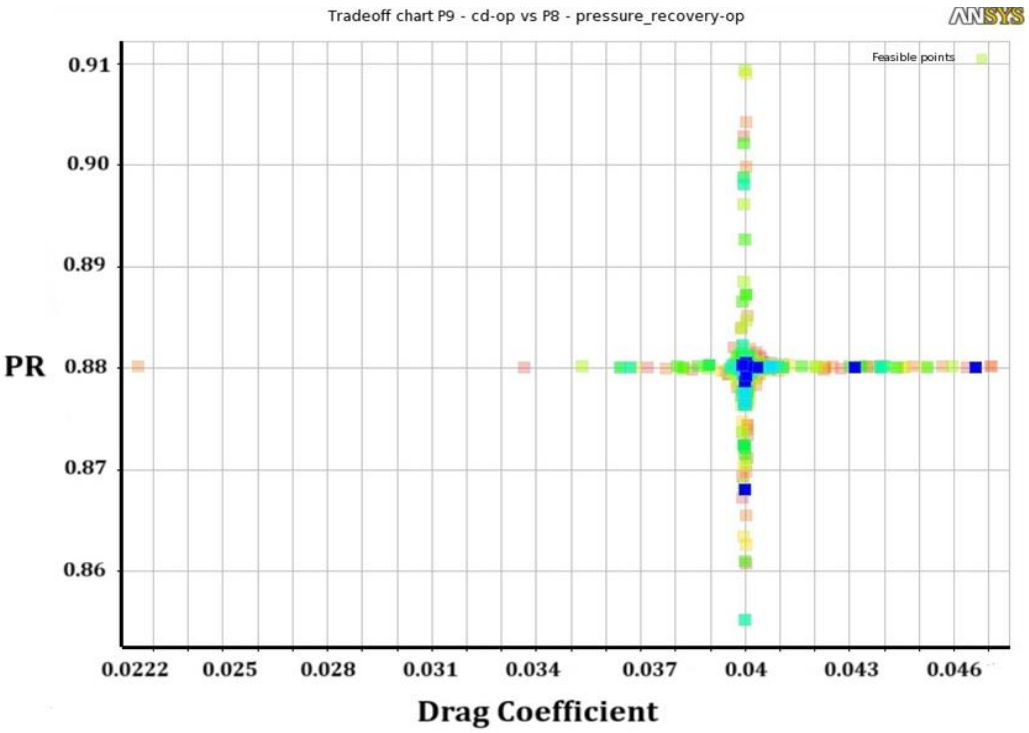

Figure 4.7. Trade-Off Chart for Climb Condition

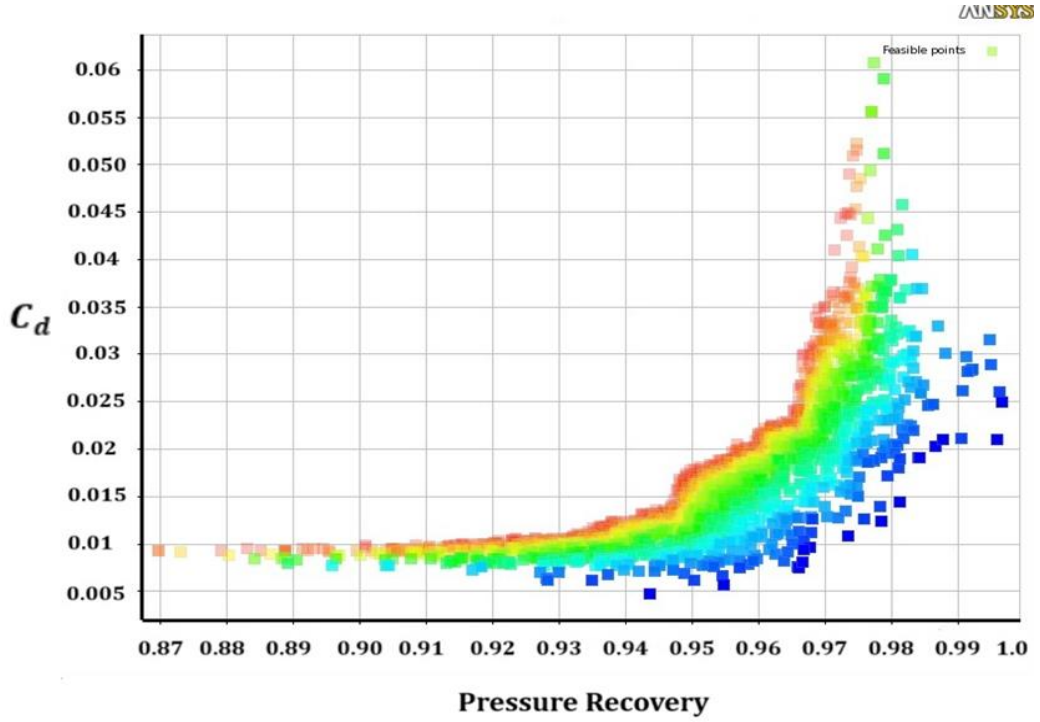

Figure 4.8. Trade-Off Chart for Climb Condition

In these figures given in previous page represent the trade-off charts of the results related to the output parameters which are pressure recovery and drag coefficient of the nacelle. To interpret Figure 4.7, points that are closer to the origin and on the Pareto-optimal curve represent the best possible designs. The green area on the figure represents the feasible design space. This is the region of the chart where achievable designs are located. Designs outside of the feasible design space are not achievable. The Pareto-optimal solutions are also shown on the chart. These are solutions that are not dominated by any other solution. In other words, no other solution can improve one objective without worsening the other. The Pareto-optimal solutions are located on the curve that bounds the feasible design space.

Within the same manner, Figure 4.8 shows the feasible design space of the iterated points. Points further away from the green area represent designs with compromises, where one objective is improved at the expense of the other. For example, even the drag coefficient drops which is a desired thing, pressure recovery also drops which is not favorable. These could be seen in colors other

than green. In points where the blue color is dominated, pressure recovery ratio reaches nearly to the maximum possible points. On the other hand, these points are not feasible for designing. Therefore, those points do not mean positive outcome. Also, points that are standing on the red area show similar behavior. Even the pressure recovery ratio of this points is higher than ones standing on feasible area, the drag coefficient of the nacelle also is higher for this section which supports the idea that one objective is improved at the expense of the other.

However, at the same pressure recovery value, the algorithm recommends points with higher drag coefficients, even if the drag coefficient is lower than that of the baseline model. The reason for this problem might be that the algorithm is stuck in a local optimum that is far from the ideal. In other words, the fact that some of the results in the analysis performed on the response surface which are far from reality may have confused the algorithm. However, as a result, the values at the feasible points suggested by the algorithm are more optimal than the baseline model.

Moreover, it could be seen in Figure 4.7 that the Pareto-optimal curve is relatively flat, which suggests that there is a significant trade-off between drag coefficient and pressure recovery meaning that it is difficult to improve one objective without sacrificing the other for climb condition. It could also be seen in candidate table that to reach the highest-pressure recovery rate, drag coefficient of the nacelle would be higher than other candidate points. In Figure 4.8, there are more points which are very close to the Pareto-optimal curve. These points represent the best possible designs, given the trade-off between output parameters.

At this point, the distribution of the high priority design output parameter pressure recovery ratio in the objective function on the fan surface is contoured for baseline model, optimal climb model and the optimal cruise model.

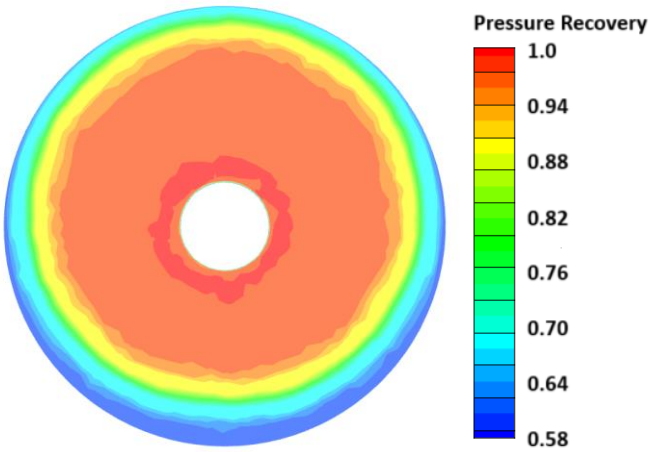

Figure 4.9. Pressure Recovery on the Fan Surface of Baseline Model for Climb

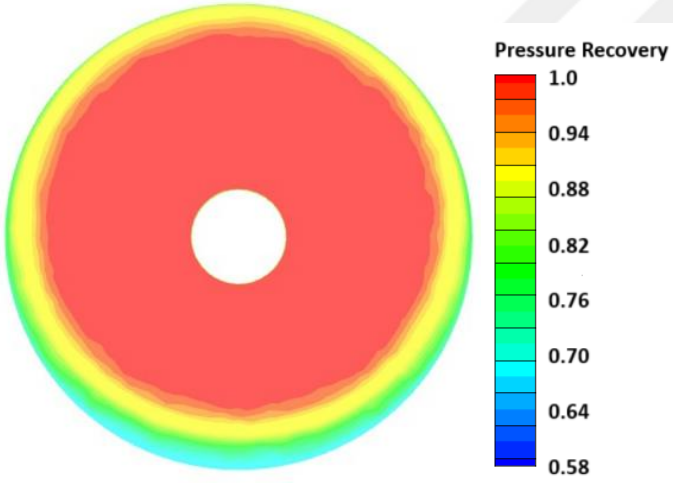

Figure 4.10. Pressure Recovery on the Fan Surface of Candidate Point 1 for Climb

Figure 4.9 and 4.10 show the total pressure recovery ratios for the baseline and the additionally analyzed Candidate Point 1 geometries at the climb condition. From these figures, the differences of pressure recovery ratios of the baseline model and the optimal model can be clearly seen. For the baseline model, the pressure recovery ratio is not distributed properly, and the abundance of blue areas is noticeable which is not sufficient. However, the pressure recovery ratio is better distributed, and the blue area region is significantly reduced in the optimal design for climb. The average pressure recovery ratio by the fan has been increased by 3.97% for the optimal model from that for the baseline model, for which the

average total pressure recovery ratios have been found as 0.9048 and 0.8702, respectively. Normally, the prediction made for the total pressure recovery ratio directly by MOGA was 0.9061. The additional CFD analysis made for the optimized shape yielded a value of 0.9048, which is very close to the MOGA prediction. This verifies that the optimization algorithm has worked properly.

With the same manner, the pressure recovery ratio distribution for the optimal design at the climb condition in comparison to the baseline one in Figures 4.11 and 4.12.

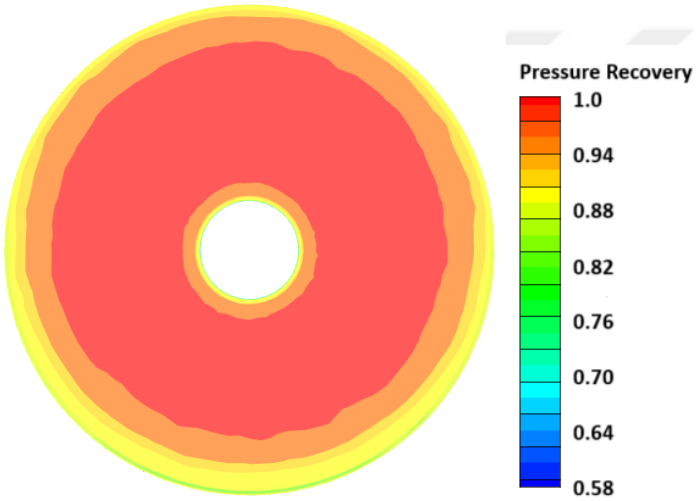

Figure 4.11. Pressure Recovery on the Fan Surface of Baseline Model for Cruise

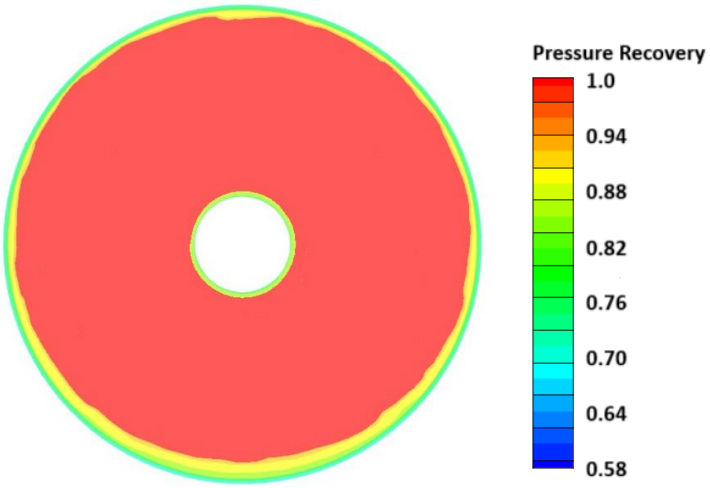

Figure 4.12. Pressure Recovery on the Fan Surface of Candidate Point 1 for Cruise

From these figures, it is observed that in comparison to the baseline model the pressure recovery ratio is distributed more properly for the optimized shape and the abundance of blue areas which correspond to lower total pressure recovery values could be eliminated to significant degree. Candidate Point Number 1 is selected again for design and the results are validated with analysis as well, as shown in Figure 4.13. All in all, the pressure recovery ratio is increased by 3.02% for the optimal model from that of the baseline model, for which the ratios are 0.9693 and 0.9408, respectively.

Although it is not one of the design objectives, it was checked whether the maximum Mach number seen on the nacelle inlet surface could be reduced with optimal design compared to the baseline model. Because in similar studies, it has been observed that the maximum Mach number on the nacelle inlet surface is reduced with optimum design [52].

In Figures 4.13 to 4.16, the candidate point number 1 is selected for comparison of the Mach number contour distributions.

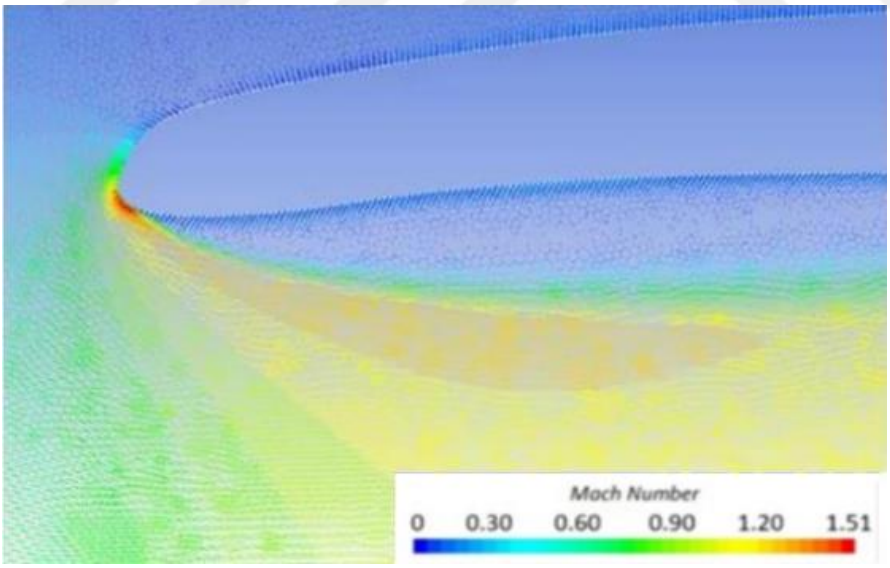

Figure 4.13. Velocity Vectors Around Inlet for Baseline Model in Climb

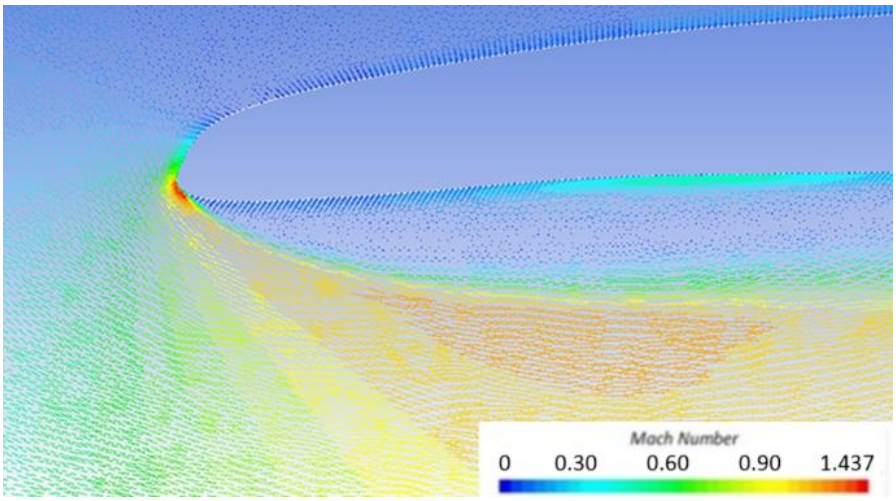

Figure 4.14. Velocity Vectors Around Inlet for Optimal Model in Climb

From Figure 4.13 and 4.14, the maximum Mach number over the initial section of the baseline and optimal nacelle is found as 1.51 and 1.437, respectively which illustrates optimal design can even decrease the maximum velocity of vectors passing over nacelle inlet. At the same time, the sections close to zero Mach number is reduced. So, the flow is distributed more smoothly.

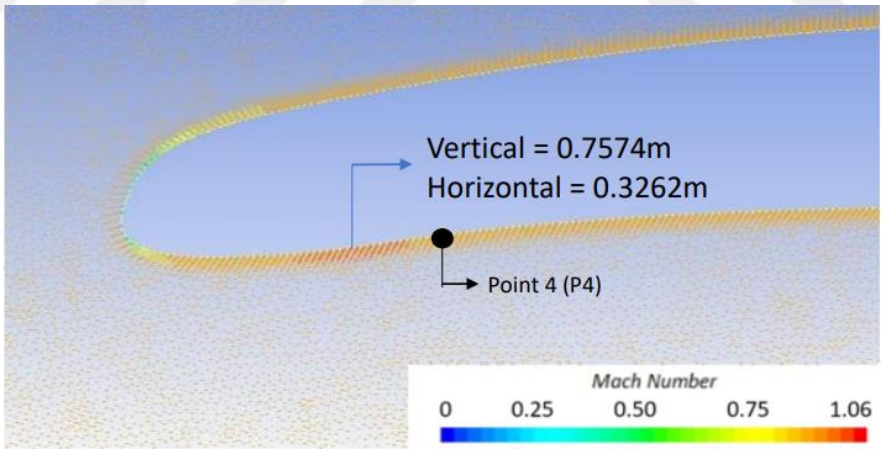

Figure 4.15. Velocity Vectors Around Inlet for Baseline Model in Cruise

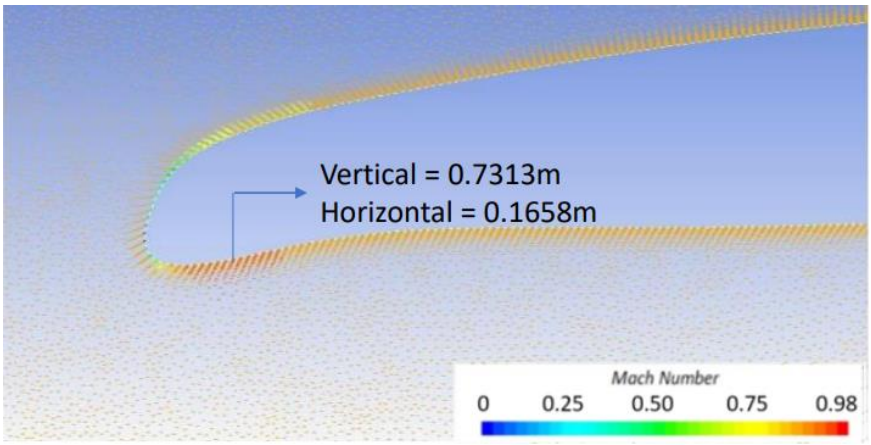

Figure 4.16. Velocity Vectors Around Inlet for Optimal Model in Cruise

Similarly, for the climb condition the maximum Mach number observed on the inlet section of the nacelle design could be improved with optimal selections of design points. From the figures it could be seen that the, the nose section curvature of the inlet is slightly inclined downwards in the optimal design that also shows similarity to the figure found in the literature [52]. Also, the location where the maximum Mach number is located is shifted backwards that also shows similarity to the figure found in the literature [52]. All in all, for the optimal design, maximum Mach number observed over the inlet section of the nacelle body drops 4.84% and 6.65% for the climb and cruise stages, respectively.

Also, the streamlines together with Mach number contours of baseline design and optimal model are given for both climb and cruise stages in Figure 4.17 to 4.20.

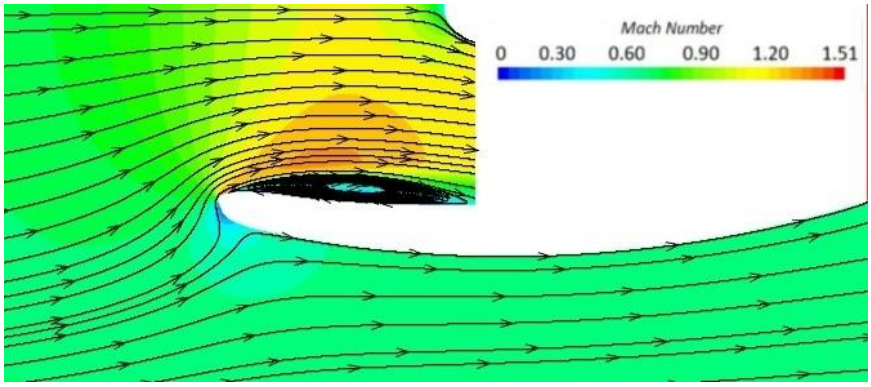

Figure 4.17. Streamlines of Baseline Design for Climb Stage

From the figure given above, streamline profiles on the baseline nacelle inlet are shown within Mach number contour for the climb stage. The circle in the figure where the flow gathers are formed due to 8° of angle of attack. The flow in this region becomes turbulent due to a phenomenon known as boundary layer separation and this separation might affect the pressure distribution of flow over the fan surface and disrupt the pressure recovery ratio on this region. Moreover, the flow separation could increase the drag coefficient of the nacelle inlet which is not a desired outcome. This is another reason for the optimization process and the results are given below.

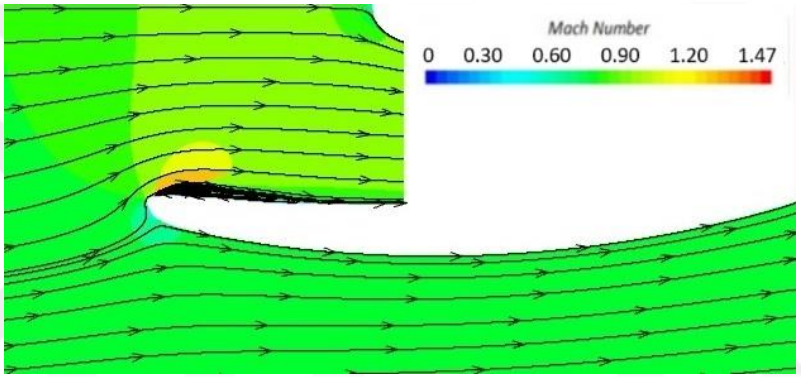

Figure 4.18. Streamlines of Optimal Design for Climb Stage

From the Figure 4.18, streamline profiles on the optimal nacelle inlet are shown within Mach number contour for the climb stage. As can be seen from the figures, the region of boundary layer separation is decreased.

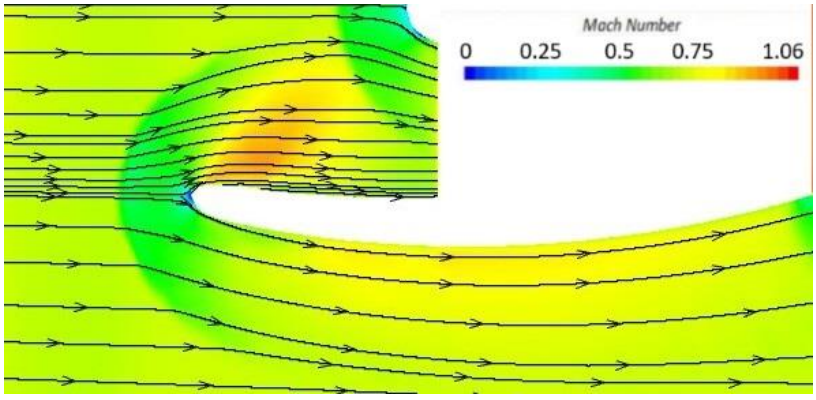

Figure 4.19. Streamlines of Baseline Design for Cruise Stage

Also, similar analyzes are made for the cruise condition and streamline figures are shown in Figure 4.19 and 4.20. Since the angle of attack value is very small, flow separation is not expected, and the graphs support this fact.

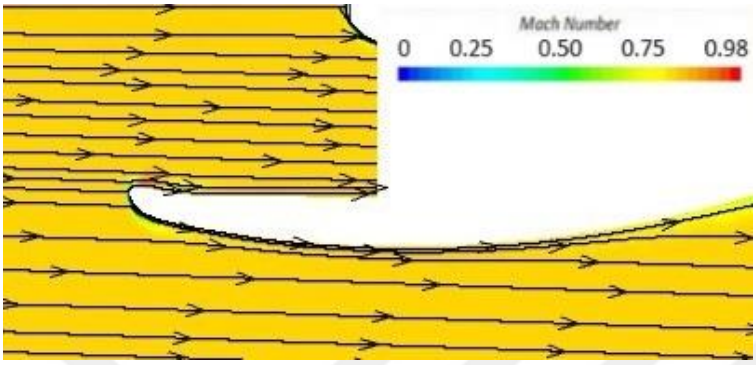

Figure 4.20. Streamlines of Optimal Design for Cruise Stage

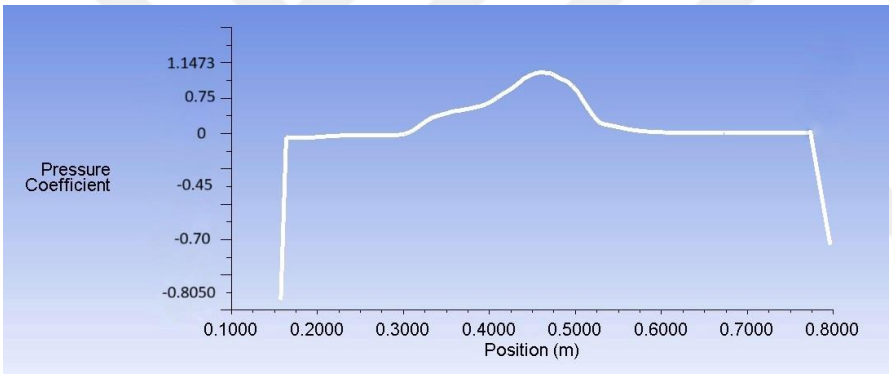

Figure 4.21. Pressure Coefficient Distribution over Fan Surface for Baseline Model (Climb)

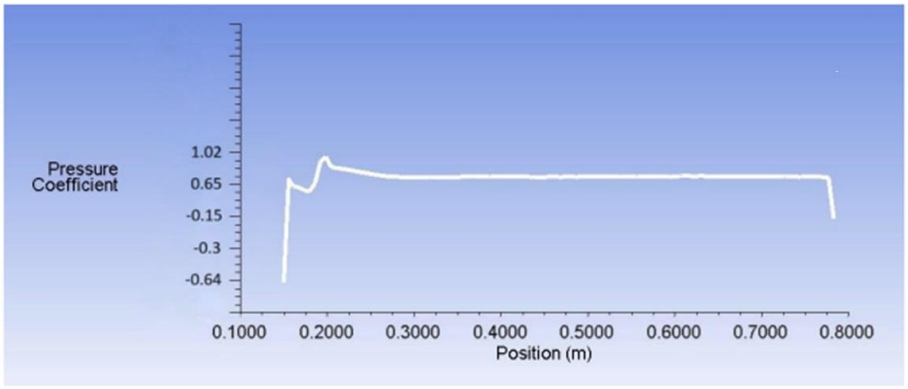

Figure 4.22. Pressure Coefficient Distribution over Fan Surface for Optimal Model (Climb)

The pressure distribution over the fan surface of both baseline and optimal nacelle body is represented in Figure 4.21 and 4.22. Although the maximum C_p value is slightly reduced in the optimal design, the distribution is smoother across the surface and the minimum pressure coefficient seen at the bottom surface of the fan is reduced by approximately 20%.

Tables 4.4 and 4.5 compare the total pressure recovery ratio and drag coefficient results from the direct MOGA analyses and the CFD analyses of the corresponding optimized shapes of the MOGA results at the climb and cruise conditions, respectively. It is observed that the estimated values made by MOGA and the verified values after additional CFD analysis are close.

Table 4.4. Verification of Candidate Points for Climb

	Pressure Recovery	**Drag Coefficient**
Candidate Point 1 (Estimated Value)	**0.9061**	**0.0432**
Candidate Point 1 (Verification Results)	**0.9048**	**0.0426**

Table 4.5. Verification of Candidate Points for Cruise

	Pressure Recovery	**Drag Coefficient**
Candidate Point 1 (Estimated Value)	**0.9712**	**0.0328**
Candidate Point 1 (Verification Results)	**0.9693**	**0.0320**

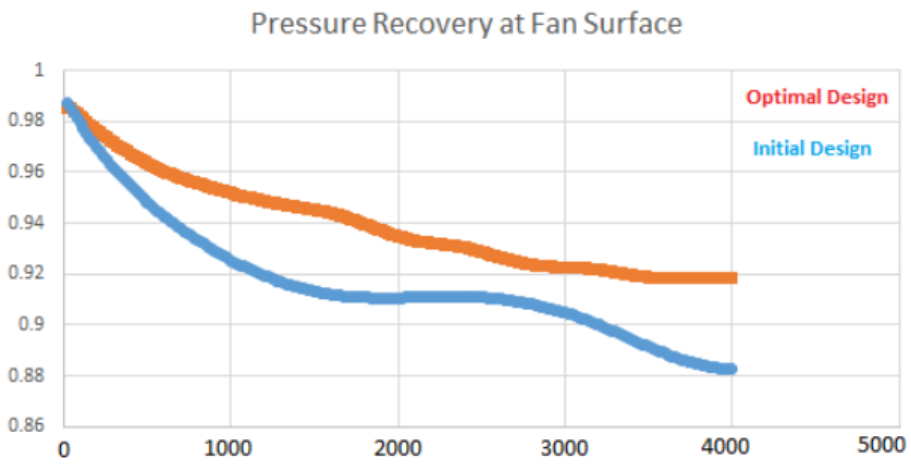

Figure 4.23. Pressure Recovery Ratio at Fan Surface Through Iteration for Climb

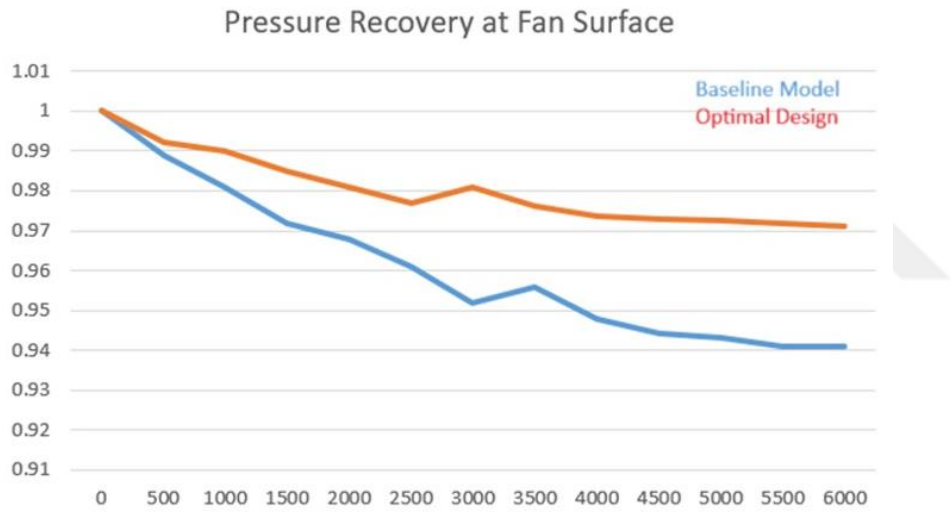

Figure 4.24. Pressure Recovery Ratio at Fan Surface Through Iteration for Cruise

Figures 4.23 and 4.24 give how the total pressure recovery ratio by the fan evolved during the iterations at the climb and cruise conditions respectively. For the convergence criterion, the pressure, momentum, energy, and turbulence equations are iterated until the convergence is reached which is selected as 10^{-5}. To satisfy the convergence criteria, nearly 4300 and 6300 iterations are made for climb and cruise stages respectively.

CHAPTER 5

CONCLUSION

In this thesis, aerodynamic shape optimization study is carried out for the air intake of a literature-based turbofan engine geometry using the total pressure recovery ratio and drag coefficient parameters into account, employing a Multi-Objective Genetic Algorithm (MOGA) fed by Reynolds-Averaged Navier-Stokes (RANS) flow solutions. A total of 7 different control points is utilized to define the baseline inlet shape. Flow solutions in the optimization study are carried out using the commercial Fluent solver using the Spalart-Allmaras turbulence model. Before optimization a verification work involving the suitability check for the mesh generation procedure, and the selected turbulence model is carried out.

Two different flight conditions are considered, namely climb and cruise. For each flight condition a total of 80 different sample nacelle shapes are created by distorting the control points of the baseline geometry, and flow solutions are obtained to form the response surface needed by the MOGA algorithm. The effects of each sample point on the output parameters are checked for understanding the behavior of each point on output parameters.

Following the verification study the optimization procedure is started by using Multi-Objective Genetic Algorithm (MOGA) to find the feasible coordinate points for each input parameter to obtain desired values on pressure recovery and drag coefficient. There is a quite difference between the results of the climb and cruise cases because trade-off charts are characteristically not the same. For climb case, Pareto optimal curve is flat which means there is a significant trade-off between pressure recovery and drag coefficient. So, it is difficult to improve one objective without sacrificing the other for climb condition. On the other hand, the curvature is kind of an exponential character for the cruise case which means at some point,

one output parameter increases even more than the other output parameter. However, in this case, there is a higher number of design points that are not feasible for construction even if they are more optimal in both parameters. Then, the candidate points are tabulated for both climb and cruise stage. In the comparison analysis, candidate point number 1 is selected for validation. Then, the pressure recovery over the fan surface of the nacelle bodies is given with related contours, where the ratios are increased by 3.97% and 3.02% for climb and cruise, respectively, from those of the baseline geometry. Also, the drag coefficients are lowered by 11.43% and 17.32% for climb and cruise, respectively. Even if the maximum Mach number is not in the objective function, the results are also checked, and shown with vector contours and streamlines where the maximum Mach number is dropped on the nacelle inlet by 4.84% and 6.65% for the climb and cruise stages of the optimal design compared to the baseline model, respectively.

Overall, the employed Multi-Objective Genetic Algorithm (MOGA) using the RANS flow solutions is shown to produce useful results in the shape optimization of the intake of a turbofan nacelle.

REFERENCES

[1] Ravindra Krishnamurthy. Engine Nacelle Aerodynamics. *GridPro Blog*. 2021.

[2] Nacelle Body. Available at https://www.quora.com/What-is-a-nacelle-in-an-aircraft-What-are-its-specific-uses-Can-it-serve-as-a-cockpit (2020).

[3] Raymer, Daniel P. *Aircraft Design: A Conceptual Approach*. American Institute of Aeronautics and Astronautics, 2006.

[4] Y. Wang, Z. Li, G. Sun. Numerical Investigation of Drag Reduction and Pressure Recovery in a Nacelle Inlet with a Variable Geometry Inlet Lip. *Aerospace Science and Technology*, 168, 2022.

[5] Ground Vorticity on Nacelle Body. Available at https://www.youtube.com/watch?v=p5l3fD2WIQc&t=1s&ab_channel=flugsnug

[6] D. Zhang, B. Li, X. Yang. A Numerical Investigation of Line Continuity in Spline-Based Nacelle Inlet Design. *Aerospace Science and Technology*, 168(107641), 2023.

[7] Wilcox, David C. (2006). *Turbulence Modeling for CFD*. DCW Industries.

[8] François G Schmitt. About Boussinesq's turbulent viscosity hypothesis: historical remarks and a direct evaluation of its validity. *Comptes Rendus Mécanique*, 335(9-10), 617-627, 2007.

[9] B. E. Launder, B. I. Sharma. Algebraic Reynolds Stress Models. *International Journal of Heat and Mass Transfer*, 17(2), 1329-1353, 1974

[10] A. A. Al-Bahar, M. K. Khan, A. A. Al-Hamed. Numerical simulation of the flow around an aircraft nacelle with a two-dimensional k-ε model. *International Journal of Heat and Fluid Flow*, 33(3), 556-567, 2012.

[11] S. H. Lee, S. W. Kang, J. H. Lee. Numerical simulation of the flow around an aircraft nacelle with the k-ω model. *Journal of Aircraft,* 47(2), 490-499, 2010.

[12] Imad Dabbura, Gradient Descent Algorithm and Its Variants. *Towards Data Science*, 2022.

[13] Sébastien Bubeck, Ronen Eldan. On the Convergence of Gradient Descent Learning Algorithms with Stochastic Gradients. *Journal of Machine Learning Research,* 8, 1123-1180, 2007.

[14] M. A. Ismail, M. A. El-Shorbagy. Stochastic Search Methods for Global Optimization. *Intelligent Data Analysis,* 299–350, 2023

[15] S. Kodiyalam, S. Baskar, R. Natarajan, R. Suresh. Surrogate Modeling for Engineering Design and Optimization. *International Journal of Modeling, Simulation, and Design,* 13(3), 143-159, 2022.

[16] A. Garzón, C. A. Ramírez-Gómez, A. P. Hernández-García. Machine Learning-Based Surrogate Modeling for Urban Water Networks: Review and Future Research Directions. *Water Resources Research*, 58(10), 2022.

[17] S. Kodiyalam, S. Baskar, R. Natarajan, R. Suresh. Surrogate Modeling for Engineering Design and Optimization. *International Journal of Modeling, Simulation, and Design,* 13(3), 143-159, 2022.

[18] C. E. Rasmussen, C. K. I. Williams. Gaussian Processes for Machine Learning, *the MIT Press*, 2006

[19] John H. Holland, Charles L. Booker, William H. Reitman. Adaptive Genetic Algorithms for Multi-Objective Optimization. *Journal of the Society for the Study of Evolution and Development,* 1978

[20] Abdullah Konak, David W. Coit, Alice E. Smith. Multi-objective optimization using genetic algorithms: A tutorial. *Reliability Engineering & System Safety,* 91(9), 2006.

[21] Deb, K. A Survey of Multiobjective Evolutionary Algorithms for Engineering Design Problems. *Journal of Genetic Programming and Evolutionary Algorithms*, 6(2), 1-34, 2011.

[22] Wang, L., Zhang, J., Chen, X. A Novel Multi-Objective Optimization Method for Structural Design Based on MOGA-ANSYS. *Computers & Structures*, 254, 112-126, 2023.

[23] Zhang, Y., Wang, Y., Chen, X. Multi-Objective Optimization of Topology and Shape of a Wing Using MOGA-ANSYS. *Journal of Aircraft*, 50(2), 1062-1072, 2023.

[24] Kalyanmoy Deb, Anirban Das. Multi-Objective Optimization Using Genetic Algorithms: A Survey of Natural Selection-Based Approaches. *IEEE Transactions on Evolutionary Computation*, 16(4), 576-601, 2012.

[25] K.S. Anisimov, A.A. Savelyev. Aerodynamic Optimization of Airplane Propulsion System within the Framework of AGILE Project. *Aerospace Science and Technology*, 64, 259-267, 2016

[26] Andrey Savelyev, Evgeniy Matyash, Andrey Shenkin. Nacelle Design and Optimization for Ultra High Bypass Ratio Turbofan. *AIP Conference Proceedings*, 1770, 020005, 2016.

[27] Li, R. and Zhong, L. Nacelle Optimization for Laminar Flow Enhancement. *Aerospace Science and Technology*, 64, 259-267, 2016

[28] C. A. Coello Coello, G. T. Pulido, E. Aguirre. A Multi-Island Genetic Algorithm for Global Optimization. *IEEE Transactions on Evolutionary Computation*, 4(3), 262-279, 2000.

[29] David W. Jones, John D. Anderson, Jr. Non-Uniform Rational B-Splines (NURBS) for Efficient Aerodynamic Design. *Journal of Aircraft*, 34(5), 1020-1027, 1997.

[30] Andrey Savelyev, Sergey Mikhaylov, Nikolay Zlenko. Nacelle Inlet Optimization for Improved Aerodynamic Performance. *Journal of Aircraft*, 56(2), 562-572, 2019.

[31] John D. Anderson, Jr., David W. Jones. Non-Uniform Rational B-Splines for Parametric Aerodynamic Design. *AIAA Journal*, 35(11):2051-2057, 1997.

[32] Wang, L., Zhang, Z., Li, H., Ma, Z. Aerodynamic Design Optimization of Nacelle/Pylon Position on an Aircraft. *Chinese Journal of Aeronautics*, 23(1), 40-49, 2010.

[33] Chen, Y., Li, X., Zhang, W. PSO-Based Optimization of Nacelle Position for Improved Aerodynamic Performance. *Chinese Journal of Aeronautics*, 28(1), 123-130, 2015.

[34] Zhang, J., Liu, X., Luo, Z. Numerical Optimization of Transonic Natural Laminar Flow Nacelles. *Journal of Aerospace Engineering*, 29(6), 2016.

[35] Storn, R., Price, K. Differential Evolution: A Practical Approach to Global Optimization. *Springer-Verlag*, 978-3-540-63065-9, 1997.

[36] Buhmann, Martin D. Radial Basis Functions for Interpolation and Approximation. *Springer-Verlag Berlin Heidelberg*, 120(3), 2000.

[37] El-Sayed, A. F., Afify, A. A., El-Shimy, M. H. Multi-Objective Optimization of Nacelle Design Using MOGA in ANSYS. *International Journal of Aerospace Engineering*, 37(1), 2014.

[38] Kumar, A., Kumar, S., Kumar, M. Multi-Objective Optimization of Nacelle-Pylon Configuration Using MOGA for Civil Aircraft. *Aerospace Science and Technology*, 73(1), 2016.

[39] Liu, X., Zhang, J., Luo, Z. Numerical Optimization of Natural Laminar Flow Airfoil for Improved Lift-to-Drag Ratio. *Aerospace Science and Technology*, 73(1), 2016.

[40] M. Goovaerts. A Review of Kriging Methods for Regression and Interpolating Complex Objective Functions. *International Journal of Mathematical Modelling and Numerical Optimization*, 1(1), 2010.

[41] Ansys, Inc. ANSYS Fluent. Available at https://www.ansys.com/products/fluids/ansys-fluent (2023).

[42] The OpenFOAM Foundation. The RANS Equations. Available at https://www.openfoam.com/documentation/guides/latest/doc/guide-turbulence-ras.html (2023)

[43] Y. Jaluria, B. Gebhart. Boussinesq's Approximation and its Application to Natural Convection Flows. *International Journal of Heat and Mass Transfer*, 16, 697-718, 1973

[44] The Spalart-Allmaras Turbulence Model. Langley Research Center. Available at https://turbmodels.larc.nasa.gov/spalart.html (2023).

[45] Launder, B. E., & Spalding, D. B. The Numerical Computation of Turbulent Flows. *Computer Methods in Applied Mechanics and Engineering*, 3(2), 269-289, 1974.

[46] Shih, T. H., Liou, W. W., Shabbir, A., Zhu, J. A New k-ε Eddy Viscosity Model for High Reynolds Number Turbulent Flows. *Computers & Fluids*, 24(3), 227-238, 1995.

[47] Ansys Fluent User Guide. Standard, RNG, and Realizable k-epsilon Models Theory.https://www.afs.enea.it/project/neptunius/docs/fluent/html/th/node57.htm (2023).

[48] Menter, F.R. Two-Equation Eddy-Viscosity Turbulence Models for Engineering Applications. *AIAA Journal*, 32(8), 1598-1605, 1994.

[49] The Menter Shear Stress Transport Turbulence Model. Langley Research Center. Available at https://turbmodels.larc.nasa.gov/sst.html (2023).

[50] Isentropic Flow Relations. National Aeronautics and Space Administration. Available at https://www.grc.nasa.gov/www/k-12/airplane/isentrop.html (2021).

[51] L. da Rocha-Schmidt, A. Hermanutz, H. Baier, A. Seitz, J. Bijewitz, A.T. Isikveren, F. Scarpa, G. Allegri, C. Remillat, E. Feuilloley, F. Majic, C. O'Reilly, G. Efraimsson, Progress Towards Adaptive Aircraft Engine Nacelles, *29th Congress of the International Council of the Aeronautical Sciences*, St. Petersburg, Russia, 2014.

[52] Frane Majić, Gunilla Efraimsson, Ciarán J. O'Reilly. Potential Improvement of Aerodynamic Performance by Morphing the Nacelle Inlet, *Aerospace Science and Technology*, 54, 235-244, 2016.

[53] Farin, G. Curves and surfaces for CAGD: A practical guide. Morgan Kaufmann, 5th Edition, 2002.

[54] Tutorials Point. Computer Graphics Curves. Available at https://www.tutorialspoint.com/computer_graphics/computer_graphics_curves.html (2023).

[55] Raymer, Daniel P. Aircraft design: A conceptual approach. 6th ed. American Institute of Aeronautics and Astronautics, 2018.

[56] Chong, E. K. P., Zak, S. H. Introduction to Optimization. *Wiley*. (p. 1), 2001.

[57] Chong, E. K. P., Zak, S. H. Introduction to Optimization. *Wiley*. (p. 216), 2001.

[58] Khan, M., Quadri, S., Nacelle Drag Prediction Using Computational Fluid Dynamics, AIAA Journal of Aircraft, 57(2), 337-348, 2020.

[59] van Dam, C.P., van Tooren, M.J.L., Drag Estimation of Nacelles for Commercial Aircraft, SAE International Journal of Aerospace, 126(1), 25-34, 2017.

[60] Myers, R. H., Montgomery, D. C., Anderson-Cook, C. M. Response Surface Methodology: Process and Product Optimization Using Designed Experiments. *Wiley*. (2009).

[61] ANSYS Tutorial: Design Optimization with Response Surface Methodology

[62] J. Wang, C. Li, and D. Zhang. Exploring the Relationship Between Design Parameters and Performance Metrics in Engineering Systems Using Correlation Scatter Plots. *Journal of Engineering Design*, 28(10-12), 789-805, 2023.

[63] James, G., Witten, D., Hastie, T., Tibshirani, R. A Tutorial on Cross-Validation. *Journal of Machine Learning Research*, 6(1), 1-47, 2005.

[64] Rosaen, K. Diagram of k-fold Cross-Validation with k = 10. *ResearchGate*. Available at https://www.researchgate.net/figure/Diagram-of-k-fold-cross-validation-with-k-10-Image-from-Karl-Rosaen-Log_fig1_332370436 (2016).

[65] Calvete, J. M., Castro, A. I., Quevedo, M. S. A New Evolutionary Algorithm for Multi-Objective Optimization Problems. *Journal of Optimization Theory and Applications*, 123(2), 201-220, 2005.

[66] Flow Chart of Multi-Objective Genetic Algorithm. Available at https://www.researchgate.net/figure/Flow-chart-of-Multi-objective-Genetic-Algorithm_fig1_28600555 (2006).

[67] Y. A. Çengel. A Simplified Approach to Bernoulli's Equation for Incompressible Flows. *Journal of Fluids Engineering*. 124(3), 620-622, 2002.

[68] National Advisory Committee for Aeronautics (NACA). The Characteristics of 78 Related Airfoil Sections from Tests in the Variable-Density Tunnel. *NACA Technical Report 460*, 1(460), 1936.

[69] NACA Technical Report 460: The Characteristics of 78 Related Airfoil Sections from Tests in the Variable-Density Tunnel. Available at https://ntrs.nasa.gov/citations/19930091108

[70] NACA Technical Report 824: Airfoil Sections for General Aviation Aircraft. Available at https://ntrs.nasa.gov/citations/19910003259

[71] CFD-Wiki. Control Volume. Available at https://www.cfd-online.com/Forums/cfx/194566-control-volume-mash-size.html

[72] Control Volume of Fluids Flow Review. Control Volume of Fluids Flow. Available at https://www.engineersedge.com/fluid_flow/control_volume.htm

[73] Ansys Inc. Ansys Fluent Meshing Guide. *Ansys Documentation*, 1(1), 2023

[74] ANSYS Inc. ANSYS Fluent User's Guide. 24.2.2 (Implicit Formulation), pages 1187-1190, 2023.

[75] Y-Plus Application in CFD Simulation. Y+ Boundary Layer Thickness. Available at https://resources.system-analysis.cadence.com/blog/msa2023-y-boundary-layer-thickness (2023).

[76] LEAP Australia & New Zealand CFD Team. LEAP Australia & New Zealand - Computational Fluid Dynamics (CFD) Blog. Available at https://www.simscale.com/forum/t/y-range-recommendations-in-documentation/77101 (2019).

[77] C.M. Chuang, K.C. Lee. Aerodynamic Performance of Nacelles for Commercial Aircraft. *American Institute of Aeronautics and Astronautics.* 37(1), 105-114, 2000.

[78] H.J. Kim, C.M. Chuang. Drag Reduction of Nacelles by Vortex Generators. *American Institute of Aeronautics and Astronautics.* 39(1), 118-126, 2002.

[79] J.H. Park, C.M. Chuang. Effect of Nacelle Shape on Aerodynamic Performance and Noise Generation. *American Institute of Aeronautics and Astronautics.* 41(1), 124-133, 2004.

PUBLICATIONS

1. Yağız Kaplan, Yusuf Özyörük, Aerodynamic Optimization of Inlet Design for High Bypass Ratio Turbofan, *12th Ankara International Aerospace Conference*, Ankara, Türkiye, September 2023.